EUROPEAN ORGANIZATION FOR NUCLEAR RESEARCH

CERN-EP/84-57
9 May 1984

MEASUREMENT OF NEUTRINO AND ANTINEUTRINO STRUCTURE FUNCTIONS IN HYDROGEN AND IRON

H. Abramowicz, G. Hansl-Kozanecki, J. May, P. Palazzi,
A. Para, F. Ranjard, A. Savoy-Navarro, D. Schlatter, J. Steinberger,
H. Taureg, W. von Rüden, H. Wahl, S. Whitaker and J. Wotschack

CERN, Geneva, Switzerland

H. Blümer, P. Buchholz, J. Duda, F. Eisele, K. Kleinknecht, J. Knobloch,
H. Lierl, B. Pszola and B. Renk

Institut für Hochenergiephysik*) der Universität Dortmund, Fed. Rep. Germany

F. Dydak, J.G.H. de Groot, T. Flottmann, C. Geweniger, V. Hepp, J. Królikowski and K. Tittel

Institut für Hochenergiephysik der Universität Heidelberg, Fed. Rep. Germany

P. Debu, C. Guyot, J.P. Merlo, P. Perez, B. Peyaud, J. Rander, J.P. Schuller and R. Turlay

DPhPE, CEN-Saclay, France

ABSTRACT

The CDHS neutrino detector has been used to measure events orginating in a tank of liquid hydrogen and in the iron of the detector. Total cross-sections, differential cross-sections, and structure functions are given for hydrogen and compared with those in iron. The measurements are in agreement with the expectations of the quark parton model. No significant differences indicative of nuclear binding effects in corresponding structure functions of protons and iron are observed. This may be of special interest in the case of the sea structure functions, since large differences are expected in some models.

(Submitted to Zeitschrift für Physik C)

---

*) Supported by the Bundesministerium für Forschung und Technologie, Bonn, Fed. Rep. Germany

1. INTRODUCTION

Deep-inelastic scattering cross-sections of neutrinos and antineutrinos in hydrogen permit the independent determination of up and down quark structure functions. Furthermore, in hydrogen these are free from the secondary effects present in complex nuclei, such as Fermi motion, and the possible collective effect of nucleons.

We present here the hydrogen experiment of the CERN–Dortmund–Heidelberg–Saclay (CDHS) Collaboration performed in the 400 GeV neutrino wide-band beam of the CERN Super Proton Synchrotron (SPS). This first neutrino hydrogen experiment using electronic techniques has certain advantages, especially at high energy, over bubble chamber experiments. The most important of these concerns the measurement of the hadron shower energy since in the H_2 bubble chamber neutral particles in general escape measurement. We report here results on total cross-sections and quark distributions in the energy range 20 to 320 GeV for neutrinos, and 20 to 160 GeV for antineutrinos.

In this experiment, neutrino and antineutrino hydrogen rates may be directly compared with the rates in the iron of the tank wall in a very similar geometry, as well as those produced in the iron modules of the muon analyser. The latter have been extensively studied to obtain iron structure functions and total cross-sections [1, 2]. Comparison of tank wall and H_2 rates makes it possible to determine the H_2 total cross-sections with a minimum of systematic uncertainty, and comparison of the tank wall rates with the main iron module rates permits checks on the systematics of the acceptance of the more complex tank geometry.

After kinematical and geometrical selection 4457 neutrino–proton and 4178 antineutrino–proton charged-current interactions are retained, as well as 2105 neutrino–iron and 1075 antineutrino–iron interactions produced in the tank wall surrounding the hydrogen target. The iron module results are based on the analysis of 50,000 neutrino and 150,000 antineutrino events.

2. PHENOMENOLOGY

The kinematical quantities measured for each event, and which define the inclusive scattering, are the following:

E_h = energy of the final hadron system;

E_ν = incident neutrino energy, the sum of the measured muon energy and E_h;

$Q^2 = -(k-k')^2$, the square of the momentum transfer to the nucleon; k and k′ are the four momenta of neutrino and muon, respectively;

$x = Q^2/2ME_h$, $0 \leq x \leq 1$;

$y = E_h/E_\nu$, $0 \leq y \leq 1$.

u, d, s and c, and $\bar{u}$, $\bar{d}$, $\bar{s}$ and $\bar{c}$ are structure functions. In the quark model they are the distributions of up, down, strange and charm quarks and antiquarks in the proton. They are functions of x and Q^2 or, alternatively, of x and E_h. It is assumed that the neutron quark distributions are those of the proton, with the interchange of u and d, and that $s(x,Q^2) = \bar{s}(x,Q^2)$ and $c(x,Q^2) = \bar{c}(x,Q^2)$.

Neglecting terms negligibly small at the energies of this experiment, the cross-sections are related to the quark distributions as follows:

$$d^2\sigma^{\nu p}/dxdy = (2xG^2ME_\nu/\pi)\,[d + s + (1-y)^2\,(\bar{u}+\bar{c}) + 1/2(1-y)q_L^{\nu p}] \quad (1)$$

$$d^2\sigma^{\bar{\nu} p}/dxdy = (2xG^2ME_\nu/\pi)\,[\bar{d} + \bar{s} + (1-y)^2(u+c) + 1/2(1-y)q_L^{\bar{\nu} p}] \quad (2)$$

$$d^2\sigma^{\nu N}/dxdy = (xG^2ME_\nu/\pi)[q + s - c + (1-y)^2(\bar{q}+\bar{c}-\bar{s}) + (1-y)q_L] \quad (3)$$

$$d^2\sigma^{\bar{\nu}N}/dxdy = (xG^2ME_\nu/\pi)[\bar{q} + \bar{s} - \bar{c} + (1-y)^2(q+c-s) + (1-y)q_L], \quad (4)$$

where $q = u + d + c + s$, $\bar{q} = \bar{u} + \bar{d} + \bar{c} + \bar{s}$, and $q_L^{\nu p}$, $q_L^{\bar{\nu}p}$ and q_L are the longitudinal quark distributions. We have put $q_L^{\nu N} = q_L^{\bar{\nu}N} = q_L$, assuming charge symmetry.

The data are obtained at fixed neutrino energy; Q^2 is therefore proportional to y. The quark distributions are functions of Q^2, and can therefore not be immediately separated on the basis of the y distributions (1) to (4). In order to extract the structure functions we first correct the cross-sections for this (small) Q^2 dependence according to quantum chromodynamics (QCD). This is dealt with in Section 6 and in the Appendix.

It must also be kept in mind that the quark distributions in iron may be affected by nuclear binding effects and are therefore not necessarily the same as those in the free nucleon.

3. EXPERIMENTAL SET-UP

3.1 Neutrino and antineutrino beams

The 400 GeV protons of the CERN SPS strike a beryllium target. The secondary hadrons are focused and sign-selected in an achromatic magnetic horn system [3]. This is followed by a 300 m long evacuated decay tunnel, and 400 m of iron- and earth-shielding. The neutrino and antineutrino spectra, as determined from charged current reaction rates, are shown in Fig. 1.

3.2 Apparatus

The neutrino beam sees successively:

i) an anticounter,
ii) a vessel containing liquid hydrogen,
iii) 15 multiwire proportional planes, and
iv) 19 magnetized iron calorimeter (MIC) modules interleaved with triple-plane drift chambers.

The layout is shown in Fig. 2.

3.2.1 Anticounter

The anticounter is composed of 16 scintillators, each of dimensions $200 \times 50 \times 2$ cm^3, covering a total surface of 4 m $\times$ 4 m, with a measured efficiency of 98%.

3.2.2 Liquid-hydrogen target

The hydrogen target (Fig. 3) is a cylindrical dewar with half-spherical end-caps. It was filled with 35 m^3 of liquid hydrogen under a mean pressure of 1.20 kg/cm^2, corresponding to a density of (0.0692 ± 0.0007) g/cm^3. The two envelopes of the hydrogen tank are made of stainless steel (Fe: 72.3%, Cr: 18%, Ni: 9.7%) of density 7.83 g/cm^3. The events produced in the tank walls are used in the analysis which follows. For these purposes it is adequate to ignore the differences in the per nucleon cross-sections of these elements. The total thickness of the end-caps is (9.25 ± 0.03) mm.

3.2.3 Vertex detector

The vertex detector consists of 5 multiwire proportional chambers, each of which contains three wire planes with 3 mm wire spacing at 120° to each other. The chambers are hexagonal, 3.75 m across flat sides.

The main technical characteristics are given in Table 1. The system is used to trigger on interactions in the tank and to reconstruct the event vertex, so that hydrogen events can be distinguished from tank wall events.

3.2.4 Magnetized iron calorimeter

The MIC is used to measure the hadron energy and the muon momentum of hydrogen tank events, and it serves as well as target and detector of neutrino events in iron. It has been used extensively to measure structure functions in iron [1, 2] and has been described in detail [4]. Each of the modules consists of circular plates 3.75 m in diameter with a total iron thickness of 75 cm. The plates are magnetized by means of a coil passing through the centre to produce a toroidal field of $\sim$ 16.5 kG. The iron plates, 5 cm thick in the front modules and 15 cm thick in the back modules, are interspersed with scintillator planes which serve to measure the energy of the hadron showers. Because of the high average density of the detector, the showers are well contained. For hydrogen tank events the hadron energy is determined on the basis of the pulse height in the first two modules (150 cm or 1180 g/cm^2 of iron). The hadron energy resolution is $\Delta E/E = 0.86/\sqrt{E(GeV)}$ [5].

The muon tracks are reconstructed on the basis of the drift-chamber measurements. Because of the focusing action of the toroidal field the typical muon traverses the entire MIC chain. The muon momentum resolution is limited by multiple scattering and is $\Delta p/p = 0.09$ on the average.

3.3 Hydrogen trigger

A hydrogen event trigger is defined in the 6 ms gate of the beam burst by the coincidence of at least seven planes of the proportional chambers, hadronic energy greater than 3.5 GeV in the MIC, and no charged particle in the veto counter. The mean efficiency of the trigger, including dead-time losses, is about 70%. The mean rate of the hydrogen trigger was 0.9 events per burst of 10^{13} protons.

4. DATA SELECTION AND CORRECTIONS

Three sets of data are selected:

i) H_2 data,
ii) iron tank wall data, and
iii) MIC data,

according to the origin of the events. The tank wall data, since the method of selection is similar to that of the H_2 data, are used to normalize the H_2 total cross-sections to the existing measurements in iron [6]. The MIC data make it possible to compare the H_2 structure functions with iron structure functions measured in the same neutrino spectrum.

The selection of the MIC events follows the method previously described [2]. The procedure for the H_2 and tank wall events is also the same for the reconstruction of the muon and the evaluation of the measured hadron shower energy. However, additional procedures are necessary for the localization of the event vertex so that the hydrogen tank wall events can be separated, and additional corrections are necessary for that part of the hadron shower energy which misses the calorimeter.

4.1 Vertex reconstruction

The vertex is reconstructed on the basis of the hits observed in the multiwire proportional chambers and the tracks reconstructed from these hits. Clearly, there must be at least one track through the chambers in addition to the muon. The event loss due to this requirement is estimated and corrected for on the basis of a

Monte Carlo calculation described further on. A typical H_2 event, before and after reconstruction, is shown in Fig. 3.

The error in the reconstructed vertex position along the beam direction is $\sim$ 2.4 cm near the downstream end of the target, which permits good separation of H_2 and tank wall events. It is 30 cm at the upbeam end. The radial uncertainty is everywhere less than 3 cm. These errors underlie the choice of the fiducial volume which is shown in Fig. 4.

In Fig. 5 a two-dimensional projection of the reconstructed event vertices is shown*). This illustrates the resolution which is achieved. It can be seen more precisely in the one-dimensional projection of Fig. 6.

4.2 Event selection

Selection criteria are introduced in order to ensure a correct event sample:

i) The muon must produce hits in at least 5 drift chambers.

ii) The hadron energy must be greater than 6 GeV.

iii) W^2, the square of the invariant mass of the final-state hadron system, must be greater than 1.166 GeV^2. This corresponds to the requirement that at least one hadron be produced, since $(m_p+m_\pi)^2 = 1.166\ GeV^2$.

iv) Muons are rejected if the reconstruction fit is not adequate, if $p_\mu > 340$ GeV, if $\theta_\mu > 0.25$, and if the distance from the track to the centre in the first chamber is greater than 1750 mm.

v) The muon must be associated with a track in the vertex chambers.

vi) The vertex must be in the fiducial region.

vii) $E_{vis} = E_h + E_\mu > 20$ GeV.

The effects of these cuts on the event sample are shown in Table 2.

4.3 Efficiency of reconstruction

The reconstruction efficiencies have been estimated by examining events which fail reconstruction. Muon reconstruction efficiency for all types of events, H_2, tank wall, and MIC, is 94%. The vertex reconstruction efficiency for H_2 and tank wall events with at least one track in addition to the muon is also 94%. The latter includes the effects of program failures as well as non-reconstructible events.

4.4 Unfolding the detector acceptance and resolution

The effects of the detector acceptance and resolution were studied and unfolded with the help of a Monte Carlo simulation. The input into this simulation consists of the following:

i) Detector geometry.

ii) Resolution of the various detector elements: hadron energy resolution, muon momentum resolution, and space resolution in the vertex detector.

iii) Neutrino spectrum. This was determined using the iron calorimeter data.

iv) The x and y distributions of the generated Monte Carlo events were chosen on the basis of existing structure function data.

v) Structure of hadron shower. A parametrization with the following properties is used:

---

*) This is, to our knowledge, the first example of neutrino radiography.

$$\langle n(\pi^+)\rangle = \langle n(\pi^-)\rangle = \langle n(\pi^0)\rangle$$

$$\langle n(K^+)\rangle = \langle n(K^-)\rangle = \langle n(K^0)\rangle = \langle n(\bar{K}^0)\rangle$$

$$\langle n_{ch}\rangle = 3.6 + 1.33 \ln W^2 - 2.43, \qquad W \text{ in GeV}$$

$$\langle n(K)\rangle/\langle n(\pi)\rangle = 0.11$$

$$\text{distribution flat in } y_i \equiv \tfrac{1}{2} \ln (E^i + p_L^i)/(E^i - p_L^i)$$

$$n(p_T^2) \propto e^{-5.7 p_T^2}.$$

This parametrization is in adequate agreement with bubble chamber results [7]. It is the basis of a correction of the order of 2 GeV in the observed hadron energy (see Fig. 7), so that the final result is not sensitive to details of this parametrization.

vi) Nuclear interaction, multiple scattering, and decay of charged secondaries before the vertex detector. These processes result in the loss of hadrons for vertex reconstruction. If all hadrons are lost, the event is lost.

Since 120,000 neutrino and an equal number of antineutrino events were generated, the statistical error introduced by this procedure is negligible. The data were corrected according to the relation C = D (G/A), where C are the corrected event numbers, D the observed event numbers, G the generated Monte Carlo event numbers, and A the accepted Monte Carlo event numbers.

To permit insight into some of the acceptance limitations of the apparatus, as well as the quality of the Monte Carlo simulation, we show in Fig. 7 the average missed hadron energy as a function of x and y, in Fig. 8 the observed and simulated vertex z distributions, in Fig. 9 the vertex R distributions, and in Fig. 10 the total energy distributions, for neutrinos and antineutrinos.

A further test of the validity of the reconstruction procedures is possible by comparing the corrected distributions for the tank wall events with those observed in the MIC. The corrections in the MIC are considerably smaller and far better understood. In Fig. 11 we show the comparison for the x distribution, and in Fig. 12 for the y distribution for the neutrino energy band $40 < E_{vis} < 160$ GeV. No differences above the statistical uncertainties are observed.

5. RESULTS

5.1 Total cross-sections

The ratio of hydrogen to tank wall events gives the cross-section ratios, after correction for geometrical efficiency differences, without the need for the knowledge of absolute neutrino flux, spectrum, dead-time, etc. The absolute proton cross-sections are then obtained using measured iron total cross-sections

$$\sigma^{\nu(\bar{\nu}),p} = \sigma^{\nu(\bar{\nu}),Fe} \,(\text{target mass Fe/target mass } H_2)\,(D_p/D_{Fe})\,(A_{Fe}/A_p)\,(G_p/G_{Fe}),$$

where D_p and D_{Fe} are the observed event numbers in hydrogen and the tank wall respectively, G_p and G_{Fe} are the generated Monte Carlo event numbers, and A_p and A_{Fe} are the corresponding Monte Carlo accepted event numbers.

The results for the ratios and for the absolute cross-sections, using world average iron cross-sections [6], are given in Table 3. These results are in good agreement with published bubble chamber results [8–11].

There is no significant energy variation. We may compare the energy averaged ratios, $\sigma^{\nu p}/\sigma^{\nu Fe} = 0.63 \pm 0.02$ and $\sigma^{\bar{\nu}p}/\sigma^{\bar{\nu}Fe} = 1.31 \pm 0.08$ with the expectations of the quark parton model. If it is assumed that up and down quark distributions are the same, then, neglecting the small strange sea contribution, and using the result $\int x(\bar{u}+\bar{d})dx/\int x(u+d)dx = 0.14$ [1] we would expect $\sigma^{\nu p}/\sigma^{\nu Fe} = 0.73$ and $\sigma^{\bar{\nu}p}/\sigma^{\bar{\nu}Fe} = 1.2$. The difference in the observed and the expected ratios can be understood when the experimentally observed difference in up and down structure functions (see Subsection 6.2) is taken into account. The observed ratio $\int xd_v dx/\int xdu_v dx$ is 0.37 ± 0.02 rather than 0.5 as was assumed in the foregoing argument. Then the quark parton model expectations become $\sigma^{\nu p}/\sigma^{\nu Fe} = 0.61$ and $\sigma^{\bar{\nu}p}/\sigma^{\bar{\nu}Fe} = 1.30$, in very good agreement with the observed total cross-section ratios. In particular, there is no indication here that the nucleon quark structure functions in a complex nucleus are disturbed by the proximity of other nucleons.

5.2 Differential cross-sections

In order to obtain the x and y dependences of the cross-sections, the energy bin 40 GeV $< E_\nu <$ 160 GeV was retained. Furthermore, those x,y bins with either excessively small acceptance ($<$ 25%) or unsmearing factor s excessively different from one ($s < 0.4, s > 1.6$) were not used in the analysis.

The cross-sections were corrected for radiation according to the method of De Rújula et al. [12] and for variation within each bin, so that the cross-sections refer to the bin centres. The results for the remaining 2787 neutrino and 2350 antineutrino hydrogen events are given in Tables 4 and 5 respectively. The results for iron obtained in the MIC modules are given in Tables 6 and 7.

6. STRUCTURE FUNCTIONS

6.1 General remarks

The data are too sparse to yield useful information on the small scaling violation effects and the small longitudinal distribution q_L. In order to extract the dominant distributions u, d, and $\bar{u}$, $\bar{d}$, it is assumed that q_L and scaling violations are adequately described by lowest order QCD. These corrections are therefore applied to the data according to the procedure described in the Appendix. The reference value of the hadron energy, for the purpose of the scaling deviations, has been taken to be 35 GeV, corresponding to $y = 0.5$. The corrected data refer then to a value of $Q^2 = 66x\ (GeV/c)^2$. The corrected cross-sections are plotted in Fig. 13. The uncorrected values are shown as well, so that the magnitude of the correction can be seen. The corrections are small enough so that the uncertainties introduced by the QCD calculations are negligible compared to the experimental errors. This is especially true in the comparison of iron and hydrogen structure functions, where these corrections are either identical as is the case for $F_2(x)$, or nearly so, as is the case for the sea structure function.

After the cross-sections are corrected for the contributions of the longitudinal structure functions and for the deviations from scaling, the structure functions are related to the cross-sections as below:

$$d^2\sigma^{\nu p}/dxdy = (2xG^2ME_\nu/\pi)\,[d + s + (1-y)^2(\bar{u}+\bar{c})] \qquad (1')$$

$$d^2\sigma^{\bar{\nu}p}/dxdy = (2xG^2ME_\nu/\pi)\,[\bar{d} + \bar{s} + (1-y)^2(u+c)] \qquad (2')$$

$$d^2\sigma^{\nu N}/dxdy = (xG^2ME_\nu/\pi)\,[q + s - c + (1-y)^2\,(\bar{q}-\bar{s}+\bar{c})] \qquad (3')$$

and

$$d^2\sigma^{\bar{\nu}N}/dxdy = (xG^2ME_\nu/\pi)[\bar{q} + \bar{s} - \bar{c} + (1-y)^2(q-s+c)]\,. \tag{4'}$$

In Eqs. (1′) to (4′) the structure functions are functions of x only, in contrast with Eqs. (1) to (4) before correction, where they were functions of Q^2 also, and therefore, indirectly, of y. The structure functions are now obtained from the cross-sections by finding the coefficients in a fit to the y distribution of the form $A + B(1-y)^2$. These fits are shown in Fig. 13 and the coefficients given in Table 8. For values of x above 0.3, it is assumed that the sea structure functions are negligibly small compared with the valence structure functions, so that the y distributions can be averaged to obtain the structure functions.

In addition to Eqs. (1′) to (4′) we have also used the relations:

$$d^2\sigma^{\nu p}/dxdy - d^2\sigma^{\bar{\nu}p}/dxdy = (2xG^2ME_\nu/\pi)\,[d_v - (1-y)^2u_v] \tag{5}$$

and

$$d^2\sigma^{\nu N}/dxdy + d^2\sigma^{\bar{\nu}N}/dxdy = (xG^2ME_\nu/\pi)\,\{(q+\bar{q})[1+(1-y)^2]\}\,, \tag{6}$$

where $u_v(x) = u - \bar{u}$ and $d_v(x) = d - \bar{d}$ are the valence quark distributions.

6.2 The up and down quark distributions and their comparison

The distributions $x[u(x)+c(x)]$ and $x[d(x)+s(x)]$ are determined from neutrino and antineutrino cross-sections respectively on the basis of Eqs. (1′) and (2′). It may be kept in mind that the contribution of s(x) is very small [13] and that of c(x) is negligible [14]. The results are shown in Fig. 14. The results for the valence quark distributions xu_v and xd_v obtained from the neutrino and antineutrino cross-section difference are shown in Fig. 15. Their ratio is shown in Fig. 16. We recall that all structure functions reported here refer to the x-dependent Q^2, $Q^2 = 66x\ (\mathrm{GeV}/c)^2$. These structure functions confirm the differences in the up and down quark distributions previously observed in charged lepton scattering experiments [15, 16] and results on neutrino and antineutrino scattering obtained in bubble chamber experiments [8–11]. Several authors have discussed the differences in the up and down quark distributions, following the observation of this difference in the SLAC experiments [15]. In particular Farrar and Jackson [17] predict that the d/u ratio should approach 0.2 at $x = 1$, whereas Field and Feynman [18] prefer the value 0 at $x = 1$. Unfortunately, as is the case also for the previous experiments, the present results do not reach sufficiently large values of x to resolve this question. The observed ratio $d_v(x)/u_v(x)$ at low values of x is close to 0.5. This is expected as a consequence of the quark sum rules [19] $\int_0^1 xu_v(x)dx/x = 2$ and $\int_0^1 xd_v(x)dx/x = 1$.

6.3 The antiquark seas $x(\bar{d}+\bar{s})$ and $x[(\bar{u}+\bar{d})/2+\bar{s}]$

As can be seen from Eq. (2′), the antiquark sea dominates antineutrino scattering at large y, and can be obtained by a fit to the antineutrino y distribution. Unfortunately, the corresponding determination of $x(\bar{u}+\bar{c})$ is not practical, because this structure function is nowhere dominant in the neutrino y distribution (1′). The $x[(\bar{u}+\bar{d})/2+\bar{s}]$ sea is obtained from the antineutrino cross-section in iron at large y. Both the $x(\bar{d}+\bar{s})$ sea as observed on the proton and the average sea $x[(\bar{u}+\bar{d})/2+\bar{s}]$ as observed in iron are shown in Fig. 17. No differences greater than experimental error are seen.

6.4 The $F_2(x)$ structure functions

By adding $xq_L(x)$ to the $y = 0$ intercept of either neutrino or antineutrino cross-sections in iron, one obtains $F_2(x) = x[q(x)+\bar{q}(x)+q_L(x)]$. The neutrino–antineutrino equality, which is expected as a consequence of charge symmetry, is experimentally verified (Fig. 18b). According to charge symmetry, the same structure function should be obtained from the proton by averaging neutrino and antineutrino $y = 0$ intercepts, after adding q_L^{ν} and $q_L^{\bar{\nu}}$ respectively. This is shown in Fig. 18a. In the absence of binding effects the proton and iron structure functions are expected to be the same.

6.5 H_2 structure functions at fixed Q^2

The structure functions reported above refer to Q^2 proportional to x, since this is the Q^2 of the measurement. It may sometimes be useful to have hydrogen structure functions available at a fixed Q^2. We therefore also give hydrogen structure functions, extrapolated on the basis of first order QCD to a common Q^2, independent of x, which we have chosen to be 15 $(GeV/c)^2$. These are given in Table 9.

7. COMPARISON OF IRON AND HYDROGEN STRUCTURE FUNCTIONS

The European Muon Collaboration (EMC) have observed [20] deviations in $F_2(x)$ as measured for iron and deuterium. This result, which corresponds to a value of $Q^2 \approx 200x$ $(GeV/c)^2$, is shown in Fig. 19a. The ratio $F_2(Fe)/F_2(D_2)$ decreases linearly from a value ~ 1.15 at small x to ~ 0.85 at the largest measured x. These deviations are confirmed at large x by SLAC electron-scattering results [21] shown in Fig. 19b. The latter refers to considerably smaller value of Q^2, $Q^2 \approx 3$–20 GeV^2, and this may be the reason for the differences in the two experiments at small x. In Fig. 19c we show the ratio $F_2(Fe)/F_2(H_2)$ found in this experiment. We might expect a similar behaviour to that observed in deuterium, since the deuterium binding effects are probably negligible compared to those in iron. We do not observe a significant deviation from unity, but given the large experimental uncertainties, the results are not in disagreement with the electron-scattering results. They seem to disagree with the EMC observations at small x. Again, this may be because the neutrino results refer to a smaller Q^2.

The EMC result has been discussed by Jaffe [22], who noted that, because of the positive deviation in the region of x in which the contribution to the quark counting sum rule is large, and because the shape of the deviation is similar to the quark–antiquark sea distributions, one should conclude that the binding effects do not perturb the valence, but rather the sea structure functions. The relative effect on the sea is then much larger, because of the smallness of the sea; an effect of the order of 1.5–2 in the ratio sea(Fe)/sea(D_2) is required to understand the EMC data. Some authors have shared this conclusion [23, 24]; others have not [25]. In Fig. 20 we show the ratio of the sea observed in iron to that in hydrogen,

$$\text{sea(Fe)/sea}(H_2) = [(\bar{u}+\bar{d})/2 + \bar{s}]_{Fe}/(\bar{d}+\bar{s})_p .$$

No significant deviation from unity is observed. For the ratio of the integrated seas,

$$\int x dx[(\bar{u}+\bar{d})/2 + \bar{s}]_{Fe}/\int x dx(\bar{d}+\bar{s})_p,$$

we find $1.10 \pm 0.11 \pm 0.07$. An effect as large as that expected by Jaffe seems to be excluded.

APPENDIX

CORRECTIONS APPLIED TO THE CROSS-SECTIONS IN ORDER TO EXTRACT THE STRUCTURE FUNCTIONS

Three corrections are applied. To the extent that the corrections require knowledge of the structure functions themselves, the process is iterative.

1. CORRECTION FOR NON-ISOSCALARITY

$$\sigma^{\nu Fe} = 30\,\sigma^{\nu n} + 26\,\sigma^{\nu p}$$

$$\sigma^{\nu N} = \tfrac{1}{2}(\sigma^{\nu n}+\sigma^{\nu p})$$

so that

$$\sigma^{\nu N} = (1/56)\,\sigma^{\nu Fe} - (1/28)(\sigma^{\nu n}-\sigma^{\nu p})$$

$$\sigma^{\nu n} - \sigma^{\nu p} = (2G^2ME_\nu\, x/\pi)[u(x)-d(x)]$$

$$\sigma^{\bar\nu n} - \sigma^{\bar\nu p} = (2G^2ME_\nu x/\pi)(1-y^2)\,[d(x)-u(x)]\,.$$

2. SUBTRACTION OF q_L

The longitudinal structure function q_L is calculated in lowest order QCD [26, 27]:

$$q_L^{\bar\nu p}(x) = (a_s/2\pi)\,x^2 \int_0^1 dz/z^2\,\{16/3\,[u(z)+c(z)+\bar d(z)+\bar s(z)] + 4f(1-x/z)\,G(z)\}$$

$$q_L^{\nu p}(x) = (a_s/2\pi)\,x^2 \int_0^1 dz/z^2\,\{16/3\,[d(z)+s(z)+\bar u(z)+\bar c(z)] + 4f(1-x/z)\,G(z)\}$$

$$q_L(x) = (a_s/2\pi)\,x^2 \int_0^1 dz/z^2\,\{8/3\,[q(z)+\bar q(z)] + 4f(1-x/z)\,G(z)\}$$

G(z) is the gluon distribution, which we have taken from an earlier paper [28].

The effective number of flavours, f, has been taken to be 3, since the energies are too low to excite the charm degree of freedom appreciably. If f is taken to be 4, the results do not change significantly.

3. CORRECTION FOR SCALING VIOLATION

The cross-sections are further corrected for the Q^2 evolution so that all y bins refer to the same Q_0^2 evaluated in the centre of the y domain, $y_0 = 0.5$; $Q_0^2 = 2Mx\langle E_\nu\rangle y_0$.

$$d^2\sigma_{corr}/dxdy = [(d^2\sigma_{meas}/dxdy) - (G^2ME_\nu/\pi)(1-y)\,xq_L]\,F(x,Q^2,Q_0^2)\,.$$

The Q^2 evolution factors

$$F^{\nu N}(x,Q^2,Q_0^2) = [q(x,Q_0^2) + (1-y)^2\bar{q}(x,Q_0^2)]/[q(x,Q^2) + (1-y)^2\bar{q}(x,Q^2)]\,,$$

$$F^{\bar{\nu}N}(x,Q^2Q_0^2) = [\bar{q}(x,Q_0^2) + (1-y)^2q(x,Q_0^2)]/[\bar{q}(x,Q^2) + (1-y)^2q(x,Q^2)]\,,$$

etc., are calculated according to the evolution equations of first order QCD [26]. At $y = 0.5$, the F's are equal to unity, of course.

REFERENCES

[1] J.G.H. Groot et al., Z. Phys. C 1 (1979) 143.
[2] H. Abramowicz et al., Z. Phys. C **17** (1983) 283.
[3] CERN Technical Report WANF SPSC T 73/7 (1983).
[4] M. Holder et al., Nucl. Instrum. Methods **148** (1978) 235.
[5] H. Abramowicz et al., Nucl. Instrum. Methods **180** (1981) 429.
[6] F. Eisele, Proc. 21st Int. Conf. on High-Energy Physics, Paris, 1982 [J. Phys. (France) **43** (1982) Suppl. 12, C3–345].
[7] N. Schmitz, Proc. Int. Symposium on Lepton and Photon Interactions at High Energies, Batavia, 1979 (FNAL, Batavia, 1979), p. 359.
[8] V.I. Efremenko et al., Phys. Lett. **84B** (1979) 511.
[9] J. Hanlon et al., Phys. Rev. Lett. **45** (1980) 1817.
[10] N. Armenise et al., Phys. Lett. **102B** (1981) 374.
[11] D. Allasia et al., Phys. Lett. **107B** (1981) 148, and **135B** (1984) 231.
[12] A. De Rújula et al., Nucl. Phys. **B154** (1979) 394.
[13] H. Abramowicz et al., Z. Phys. C **15** (1982) 19.
[14] H. de Groot et al., Phys. Lett. **86B** (1979) 103.
[15] A. Bodek et al., Phys. Rev. **D20** (1979) 1471.
P. Allen et al., Phys. Lett. **103B** (1981) 71.
[16] J.J. Aubert et al., Phys. Lett. **123B** (1983) 123.
[17] G.R. Farrar and D.R. Jackson, Phys. Rev. Lett. **35** (1975) 1416.
[18] R.D. Field and R.P. Feynman, Phys. Rev. **D15** (1977) 2590.
[19] D.J. Gross and C.H. Llewellyn Smith, Nucl. Phys. **B14** (1969) 337.
[20] J.J. Aubert et al., Phys. Lett. **123B** (1983) 275.
[21] A. Bodek et al., Phys. Rev. Lett. **50** (1983) 1431 and **51** (1983) 534.
[22] R.L. Jaffe, Phys. Rev. Lett. **50** (1983) 228.
[23] C.H. Llewellyn Smith, Phys. Lett. **128B** (1983) 107.
[24] M. Ericson and A.W. Thomas, Phys. Lett. **128B** (1983) 112.
[25] H. Faissner and B.R. Kim, Phys. Lett. **130B** (1983) 321.
[26] See, for example, G. Altarelli, Phys. Rep. **81** (1982) 53.
[27] A. Zee, F. Wilczek and S.B. Treiman, Phys. Rev. **D10** (1974) 2881.
I. Hinchliffe and C.H. Llewellyn Smith, Nucl. Phys. **B128** (1977) 93.
G. Altarelli and G. Martinelli, Phys. Lett. **76B** (1978) 89.
[28] H. Abramowicz et al., Z. Phys. **C12** (1982) 289.

Table 1

Characteristics of the vertex detector

5 multiwire proportional chambers of hexagonal shape, width 3.7 m	
3-coordinate planes at 120°	
Number of wires per plane	1232
Distance between wires	3 mm
Wire diameter	30×10^{-3} mm
Gap between wires and high-voltage graphited planes	10 mm
High voltage	−3800 V
Gas mixture	argon 80% isobutane 20% freon 0.05%
Read-out	FILAS circuits (EFCIS Grenoble)
Efficiency of one plane	97%

Table 2

Effect of different data cuts on event numbers

	ν	$\bar{\nu}$
Protons on target	1.6×10^{18}	4.5×10^{18}
Registered events	208500	342200
Events processed with $E_H > 3$ GeV	81038	78765
Cuts and rejects		
· At least 5 drift chambers hit	38425	33170
· $E_H < 6$ GeV, $W^2 < 1.166$	19564	26739
· Rejected muons (not found, bad fit, $p_\mu > 340$ GeV, wrong sign, large radius $R_\mu > 1750$, $\theta_\mu > 0.250$, more than 1 μ)	6656	7826
· Rejected vertices in tank (no vertex, less than 2 tracks, less than 7 hits in MWPC μ not associated with MWPC, vertices outside fiducial volume)	8771	4771
· $E_{vis} < 20$ GeV	1060	1006
Selected events		
Hydrogen	4457	4178
Iron tank wall	2105	1075

Table 3

Ratio of cross-sections in iron relative to cross-sections in hydrogen for neutrinos and antineutrinos. Values of cross-sections in hydrogen are derived assuming $\sigma^{\nu Fe}/E_\nu = 0.625 \times 10^{-38}$ cm^2/GeV and $\sigma^{\bar{\nu}Fe}/E_{\bar{\nu}} = 0.3 \times 10^{-38}$ cm^2/GeV.

	Energy bin (GeV)		Number of events hydrogen (iron)	Acceptance correction (Monte Carlo estimate) corr. H_2/corr. Fe	σ^p/σ^{Fe}	σ^p/E_ν (10^{-38} cm^2/GeV)
ν	20	40	1362 (706)	1.27	0.63 ± 0.03 ± 0.05	0.394 ± 0.019 ± 0.037
	40	80	1497 (696)	1.18	0.63 ± 0.03 ± 0.02	0.394 ± 0.019 ± 0.023
	80	160	1290 (578)	1.05	0.62 ± 0.03 ± 0.05	0.388 ± 0.019 ± 0.037
	160	320	308 (125)	1.00	0.61 ± 0.07 ± 0.12	0.381 ± 0.044 ± 0.077
$\bar{\nu}$	20	40	1828 (487)	1.38	1.39 ± 0.07 ± 0.09	0.417 ± 0.021 ± 0.036
	40	80	1582 (393)	1.24	1.29 ± 0.08 ± 0.07	0.387 ± 0.024 ± 0.029
	80	160	768 (195)	1.17	1.26 ± 0.11 ± 0.14	0.378 ± 0.033 ± 0.046

Table 4

Differential cross-section for neutrino–hydrogen interactions $(1/E_\nu)(d^2\sigma^{\nu p}/dxdy)$.
$40 < E_\nu < 160$ GeV, $\langle E_\nu \rangle = 80$ GeV. First error statistical, second error systematical. Units are 10^{-38} cm^2/GeV.

y	x = 0.05	x = 0.15	x = 0.25	x = 0.35	x = 0.45	x = 0.55	x = 0.65
0.15	1.317 ± 0.136 ± 0.16	1.366 ± 0.141 ± 0.10	0.953 ± 0.118 ± 0.08	0.556 ± 0.087 ± 0.07	0.410 ± 0.069 ± 0.07	0.174 ± 0.044 ± 0.06	
0.25	1.388 ± 0.125 ± 0.12	1.266 ± 0.123 ± 0.10	0.775 ± 0.097 ± 0.07	0.663 ± 0.09 ± 0.06	0.385 ± 0.069 ± 0.06	0.227 ± 0.050 ± 0.04	0.077 ± 0.022 ± 0.04
0.35	1.491 ± 0.135 ± 0.11	1.265 ± 0.122 ± 0.09	0.682 ± 0.091 ± 0.07	0.458 ± 0.074 ± 0.05	0.36 ± 0.065 ± 0.05	0.165 ± 0.041 ± 0.04	0.071 ± 0.022 ± 0.03
0.45	1.170 ± 0.115 ± 0.10	0.905 ± 0.101 ± 0.07	0.809 ± 0.097 ± 0.07	0.523 ± 0.080 ± 0.05	0.372 ± 0.070 ± 0.05	0.122 ± 0.036 ± 0.03	0.044 ± 0.019 ± 0.02
0.55	1.276 ± 0.115 ± 0.10	1.105 ± 0.110 ± 0.07	0.698 ± 0.091 ± 0.06	0.387 ± 0.069 ± 0.04	0.248 ± 0.057 ± 0.04	0.109 ± 0.032 ± 0.03	0.058 ± 0.023 ± 0.02
0.65	1.000 ± 0.099 ± 0.10	0.885 ± 0.101 ± 0.05	0.751 ± 0.096 ± 0.05	0.378 ± 0.07 ± 0.05	0.180 ± 0.052 ± 0.04	0.095 ± 0.035 ± 0.03	0.044 ± 0.020 ± 0.02
0.75	0.999 ± 0.104 ± 0.08	0.898 ± 0.106 ± 0.05	0.734 ± 0.104 ± 0.05	0.331 ± 0.073 ± 0.06	0.155 ± 0.059 ± 0.06		
0.85	0.775 ± 0.11 ± 0.08	1.060 ± 0.131 ± 0.08	0.725 ± 0.121 ± 0.08	0.473 ± 0.123 ± 0.08			

Table 5

Differential cross-section for antineutrino interactions in hydrogen $(1/E_{\bar{\nu}})(d^2\sigma^{\bar{\nu}p}/dxdy)$.
$40 < E_\nu < 160$ GeV, $\langle E_\nu \rangle = 70$ GeV.

y	x = 0.05	x = 0.15	x = 0.25	x = 0.35	x = 0.45	x = 0.55	x = 0.65
0.15	1.589 ± 0.156 ± 0.16	1.677 ± 0.172 ± 0.16	1.173 ± 0.134 ± 0.12	1.357 ± 0.166 ± 0.12	0.999 ± 0.121 ± 0.10	0.549 ± 0.093 ± 0.10	
0.25	1.563 ± 0.142 ± 0.12	1.385 ± 0.137 ± 0.10	1.220 ± 0.131 ± 0.10	1.157 ± 0.132 ± 0.10	0.620 ± 0.093 ± 0.08	0.395 ± 0.074 ± 0.06	0.102 ± 0.031 ± 0.04
0.35	1.250 ± 0.124 ± 0.10	1.228 ± 0.122 ± 0.08	0.786 ± 0.100 ± 0.08	0.649 ± 0.097 ± 0.08	0.355 ± 0.069 ± 0.06	0.178 ± 0.048 ± 0.05	0.152 ± 0.039 ± 0.04
0.45	1.143 ± 0.117 ± 0.10	0.732 ± 0.094 ± 0.08	0.596 ± 0.087 ± 0.08	0.400 ± 0.071 ± 0.06	0.415 ± 0.082 ± 0.06	0.136 ± 0.045 ± 0.05	0.056 ± 0.027 ± 0.03
0.55	0.781 ± 0.095 ± 0.07	0.708 ± 0.088 ± 0.07	0.521 ± 0.079 ± 0.06	0.324 ± 0.066 ± 0.04	0.181 ± 0.05 ± 0.03	0.081 ± 0.032 ± 0.02	0.031 ± 0.022 ± 0.02
0.65	0.604 ± 0.077 ± 0.06	0.534 ± 0.079 ± 0.06	0.231 ± 0.053 ± 0.05	0.132 ± 0.039 ± 0.04	0.126 ± 0.044 ± 0.04	0.043 ± 0.024 ± 0.02	
0.75	0.759 ± 0.094 ± 0.06	0.385 ± 0.07 ± 0.06	0.248 ± 0.054 ± 0.05	0.111 ± 0.042 ± 0.03			
0.85	0.608 ± 0.088 ± 0.06	0.325 ± 0.073 ± 0.06	0.165 ± 0.058 ± 0.04	0.064 ± 0.045 ± 0.03			

Table 6

Differential cross-section for neutrino–iron interactions in iron core magnet.
$40 < E_\nu < 160$ GeV, bin centred $\langle E_\nu \rangle = 70$ GeV.

y	x = 0.05	x = 0.15	x = 0.25	x = 0.35	x = 0.45	x = 0.55	x = 0.65
0.15	1.571 ± 0.086	1.872 ± 0.101	1.518 ± 0.090	1.072 ± 0.073	0.770 ± 0.062	0.402 ± 0.042	–
0.25	1.753 ± 0.090	1.604 ± 0.088	1.370 ± 0.083	1.035 ± 0.071	0.588 ± 0.051	0.368 ± 0.039	–
0.35	1.505 ± 0.080	1.597 ± 0.087	1.379 ± 0.082	0.982 ± 0.069	0.541 ± 0.048	0.343 ± 0.037	0.149 ± 0.017
0.45	1.517 ± 0.080	1.656 ± 0.088	1.342 ± 0.080	1.025 ± 0.071	0.618 ± 0.054	0.320 ± 0.036	0.118 ± 0.016
0.55	1.474 ± 0.077	1.530 ± 0.083	1.208 ± 0.075	0.823 ± 0.061	0.534 ± 0.051	0.252 ± 0.032	0.093 ± 0.014
0.65	1.347 ± 0.073	1.558 ± 0.083	1.213 ± 0.074	0.860 ± 0.064	0.548 ± 0.050	0.293 ± 0.035	0.093 ± 0.014
0.75	1.324 ± 0.072	1.597 ± 0.085	1.325 ± 0.079	0.851 ± 0.063	0.519 ± 0.049	0.176 ± 0.026	0.061 ± 0.011
0.85	1.379 ± 0.076	1.459 ± 0.084	1.209 ± 0.076	0.840 ± 0.065	0.545 ± 0.054	0.229 ± 0.032	0.090 ± 0.015

Table 7

Differential cross-section for antineutrino–iron interactions in iron core magnet.
$40 < E_\nu < 160$ GeV, bin centred $\langle E_\nu \rangle = 70$ GeV.

y	x = 0.05	x = 0.15	x = 0.25	x = 0.35	x = 0.45	x = 0.55	x = 0.65
0.15	1.302 ± 0.038	1.429 ± 0.043	1.032 ± 0.035	0.811 ± 0.032	0.479 ± 0.022	0.264 ± 0.015	–
0.25	1.226 ± 0.036	1.166 ± 0.037	0.851 ± 0.031	0.550 ± 0.024	0.338 ± 0.018	0.199 ± 0.013	0.077 ± 0.005
0.35	1.145 ± 0.034	0.918 ± 0.030	0.658 ± 0.025	0.399 ± 0.019	0.262 ± 0.015	0.123 ± 0.010	0.044 ± 0.005
0.45	0.918 ± 0.029	0.767 ± 0.027	0.469 ± 0.020	0.293 ± 0.015	0.180 ± 0.012	0.075 ± 0.007	0.038 ± 0.003
0.55	0.833 ± 0.027	0.605 ± 0.023	0.378 ± 0.017	0.212 ± 0.012	0.103 ± 0.008	0.059 ± 0.007	0.021 ± 0.003
0.65	0.755 ± 0.025	0.498 ± 0.020	0.282 ± 0.014	0.131 ± 0.009	0.064 ± 0.007	0.036 ± 0.005	0.014 ± 0.003
0.75	0.625 ± 0.022	0.396 ± 0.017	0.178 ± 0.011	0.085 ± 0.007	0.042 ± 0.005	0.014 ± 0.003	0.011 ± 0.002
0.85	0.540 ± 0.021	0.330 ± 0.016	0.141 ± 0.010	0.043 ± 0.005	0.021 ± 0.003	0.007 ± 0.002	–

Table 8

Results of the fit of hydrogen data at $E_h = 35$ GeV, corrected as indicated in the Appendix.
Above $x = 0.3$, d_v, u_v and d_v/u_v are obtained assuming no sea.

x	$x(d+s)$	$x(\bar{d}+\bar{s})$	$x(u+c)$	xd_v	xu_v	d_v/u_v
0.05	$0.239 \pm 0.019 \pm 0.008$	$0.127 \pm 0.017 \pm 0.010$	$0.465 \pm 0.065 \pm 0.060$	0.109 ± 0.025	0.207 ± 0.084	$0.524 \pm 0.150 \pm 0.140$
0.15	$0.276 \pm 0.021 \pm 0.009$	$0.082 \pm 0.015 \pm 0.010$	$0.568 \pm 0.058 \pm 0.060$	0.198 ± 0.026	0.416 ± 0.089	$0.476 \pm 0.068 \pm 0.090$
0.25	$0.234 \pm 0.020 \pm 0.009$	$0.041 \pm 0.012 \pm 0.008$	$0.442 \pm 0.046 \pm 0.050$	0.192 ± 0.024	0.462 ± 0.063	$0.417 \pm 0.025 \pm 0.070$
0.35	$0.124 \pm 0.016 \pm 0.009$	$-0.004 \pm 0.010 \pm 0.008$	$0.484 \pm 0.044 \pm 0.050$	0.142 ± 0.009	0.472 ± 0.031	$0.296 \pm 0.028 \pm 0.060$
0.45	$0.063 \pm 0.013 \pm 0.009$	$-0.001 \pm 0.016 \pm 0.010$	$0.311 \pm 0.044 \pm 0.040$	0.090 ± 0.007	0.308 ± 0.024	$0.299 \pm 0.034 \pm 0.050$
0.55	$0.033 \pm 0.010 \pm 0.009$	$-0.011 \pm 0.009 \pm 0.012$	$0.181 \pm 0.030 \pm 0.040$	0.042 ± 0.005	0.152 ± 0.016	$0.287 \pm 0.046 \pm 0.060$
0.65	$0.014 \pm 0.007 \pm 0.007$	$0.005 \pm 0.009 \pm 0.012$	$0.043 \pm 0.019 \pm 0.020$	0.018 ± 0.013	0.052 ± 0.008	$0.253 \pm 0.068 \pm 0.070$

Table 9

The hydrogen structure functions $x(\bar{d}+\bar{s})$, $x(u+c)$, $x(d+s)$, xu_v, and xd_v, renormalized on the basis of QCD to the x independent value of Q^2, $Q^2 = 15\ (GeV/c)^2$.

x	x(d+s)	$x(\bar{d}+\bar{s})$	x(u+c)	xd_v	xu_v
0.05	0.292 ± 0.023	0.150 ± 0.019	0.574 ± 0.078	0.136 ± 0.032	0.253 ± 0.014
0.15	0.277 ± 0.021	0.081 ± 0.015	0.576 ± 0.058	0.201 ± 0.027	0.426 ± 0.091
0.25	0.235 ± 0.020	0.042 ± 0.012	0.449 ± 0.046	0.193 ± 0.024	0.465 ± 0.061
0.35	0.132 ± 0.017	−0.003 ± 0.011	0.514 ± 0.047	0.152 ± 0.009	0.504 ± 0.032
0.45	0.072 ± 0.015	−0.001 ± 0.018	0.353 ± 0.050	0.103 ± 0.008	0.352 ± 0.027
0.55	0.042 ± 0.012	−0.013 ± 0.012	0.224 ± 0.037	0.053 ± 0.006	0.189 ± 0.020
0.65	0.020 ± 0.010	0.007 ± 0.013	0.060 ± 0.027	0.026 ± 0.004	0.073 ± 0.011

Figure captions

Fig. 1 : Neutrino and antineutrino beam spectra as measured in the MIC.

Fig. 2 : Layout of the detector.

Fig. 3 : Typical hydrogen event a) before and b) after reconstruction.

Fig. 4 : Cross-section through the hydrogen dewar vessel. The fiducial volume is indicated.

Fig. 5 : Neutrinogram of the target. Two-dimensional projection of the vertex distribution of reconstructed events.

Fig. 6 : One-dimensional, radial projection of the events of the previous figure.

Fig. 7 : Calculated average geometrical hadron energy loss for hydrogen events as a function of y, for $E_\nu = 70$ GeV.

Fig. 8 : Comparison of the z distribution of the data with the Monte Carlo calculation.

Fig. 9 : Comparison of the radial distribution of the data with the Monte Carlo calculation.

Fig. 10 : Comparison of the visible energy distribution ($E_{vis} = E_{had} + E_\mu$) with the Monte Carlo calculation.

Fig. 11 : Comparison of the x distributions observed in the tank wall and in the MIC.

Fig. 12 : Comparison of the y distributions observed in the tank wall and in the MIC.

Fig. 13 : y distributions for different x bins, dots before, crosses after correction for q_L and scaling violation. The fits to the form $A + B(1-y)^2$ are also shown. a) Neutrino results; b) antineutrino results.

Fig. 14 : a) The up quark distribution $x[u(x)+c(x)]$. b) The down quark distribution $x[d(x)+s(x)]$.

Fig. 15 : a) The valence up quark distribution $xu_v(x)$. b) The valence down quark distribution $xd_v(x)$.

Fig. 16 : $d_v(x)/u_v(x)$.

Fig. 17 : a) The down quark sea x, $[\bar{d}(x) + \bar{s}(x)]$ of the proton.
b) The average sea $x\{[\bar{u}(x)+\bar{d}(x)]/2 + \bar{s}(x)\}$ of iron.

Fig. 18 : a) $F_2(x)$ of the proton obtained from the average of the neutrino and the antineutrino cross-section at $y = 0$. b) $F_2(x)$ of iron independently from neutrino and antineutrino cross-sections at $y = 0$.

Fig. 19 : The ratio $F_2(Fe)/F_2(D_2)$: a) as observed in muon-scattering experiments [20] and b) as observed in electron-scattering experiments [21], and c) the ratio $F_2(Fe)/F_2(H_2)$ as observed in this experiment.

Fig. 20 : The ratio of the sea distributions in iron and hydrogen, $[(\bar{u}+\bar{d})/2 + \bar{s}]_{Fe}/(\bar{d}+\bar{s})_p$.

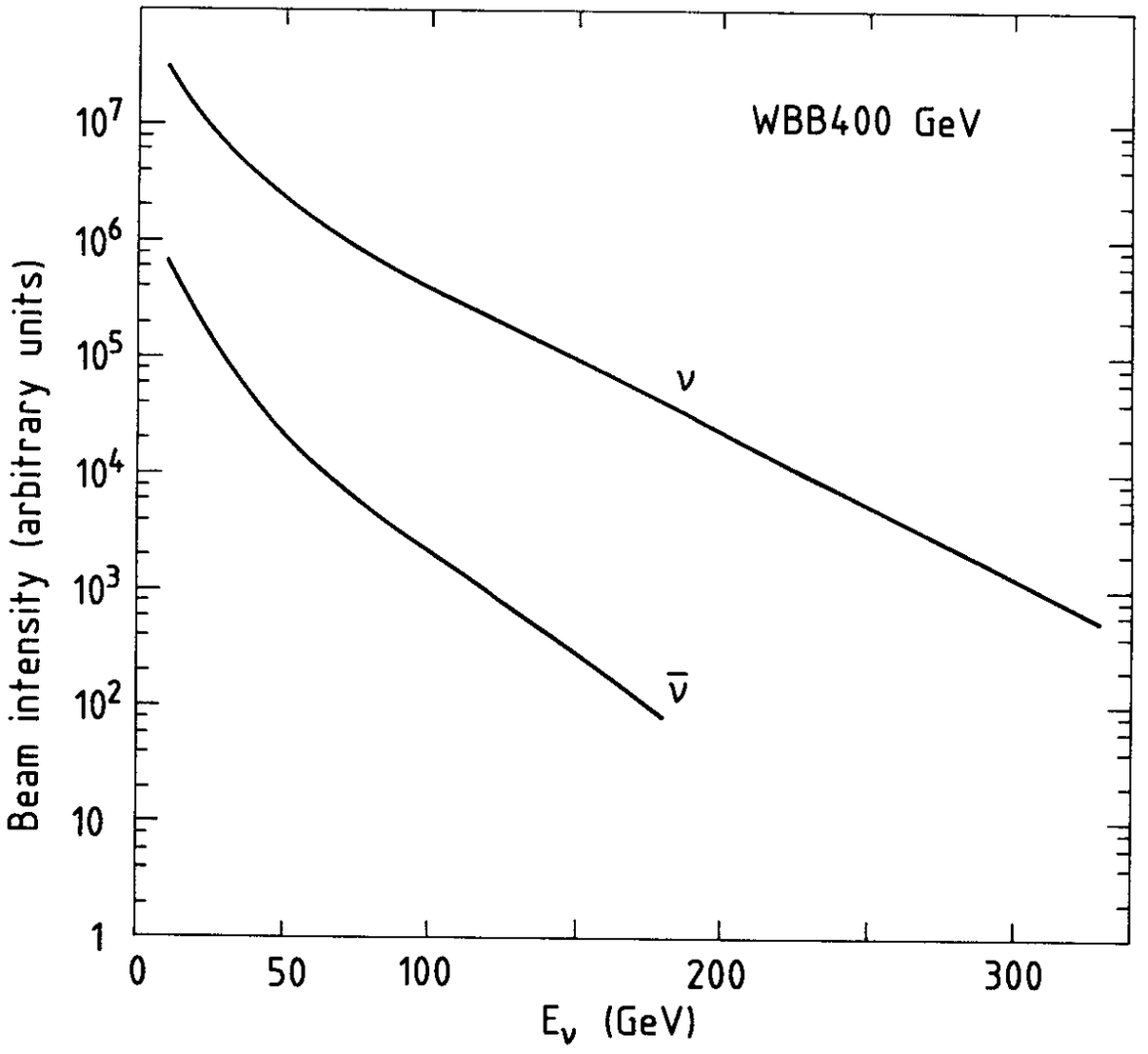
WBB400 GeV
Beam intensity (arbitrary units)
10^7
10^6
10^5
10^4
10^3
10^2
10
1
0
50
100
200
300
E_ν (GeV)
ν
$\bar{\nu}$

Fig. 1

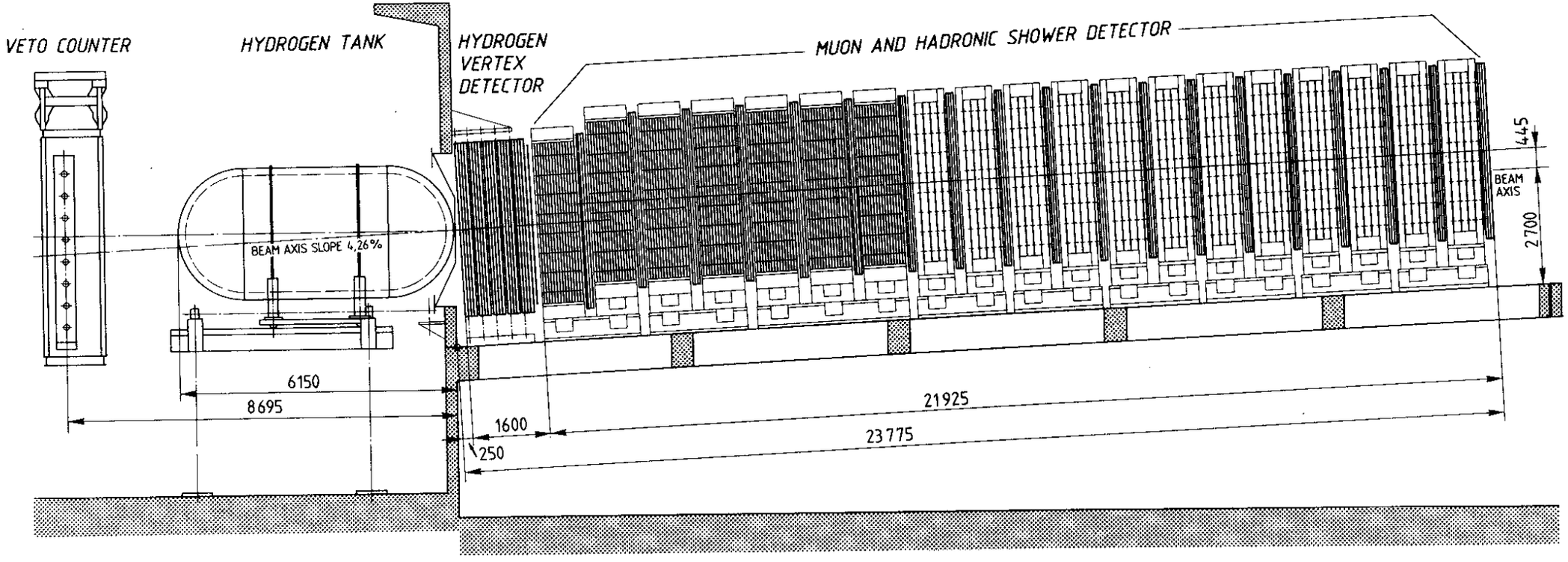
VETO COUNTER
HYDROGEN TANK
HYDROGEN VERTEX DETECTOR
MUON AND HADRONIC SHOWER DETECTOR
BEAM AXIS SLOPE 4,26%
445
BEAM AXIS
2700
6150
8695
1600
21925
23775
250

Fig. 2

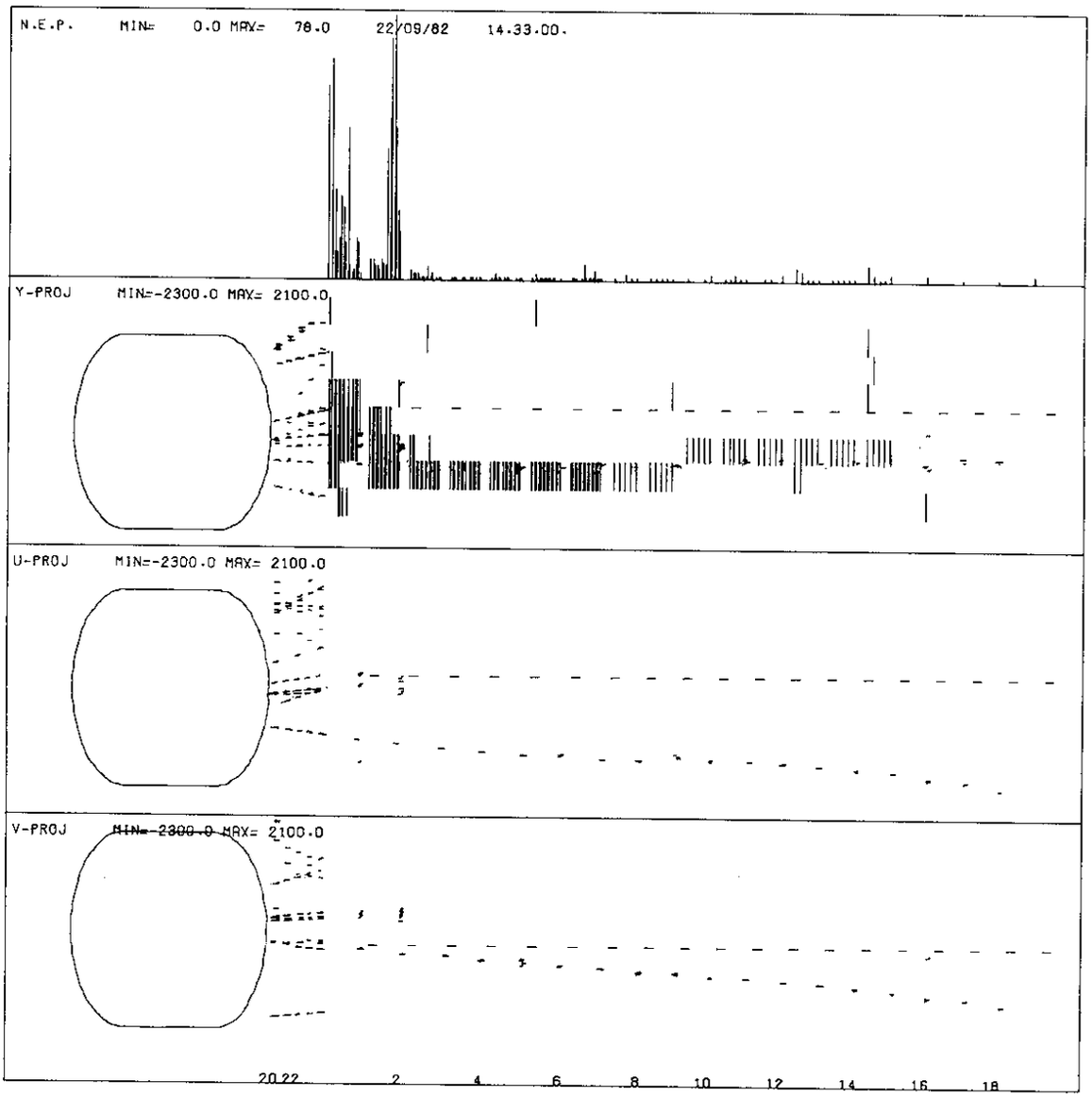
N.E.P. MIN= 0.0 MAX= 78.0 22/09/82 14.33.00.
Y-PROJ MIN=-2300.0 MAX= 2100.0
U-PROJ MIN=-2300.0 MAX= 2100.0
V-PROJ MIN=-2300.0 MAX= 2100.0
20 22 2 4 6 8 10 12 14 16 18

Fig.3a

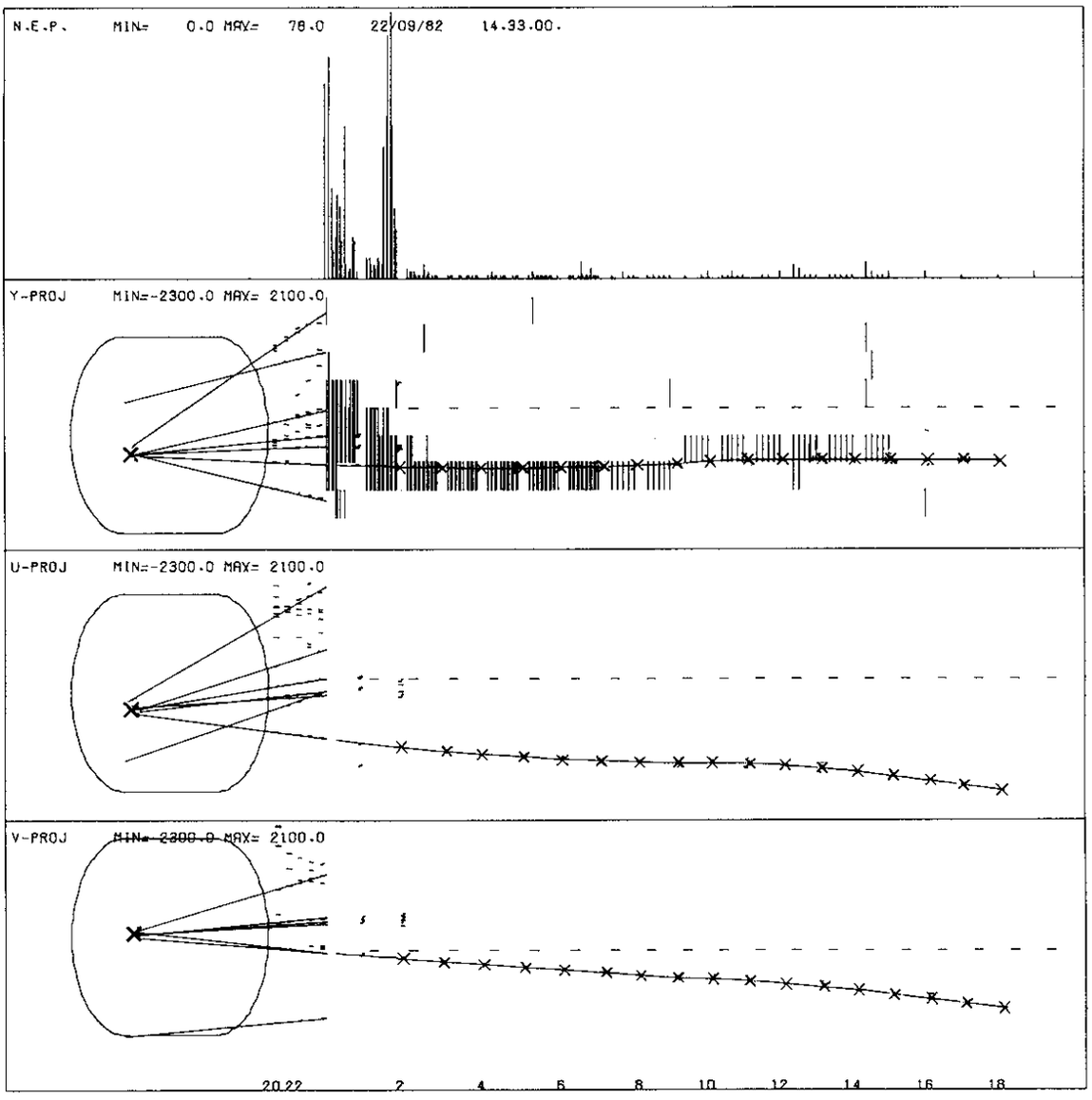
N.E.P.
MIN= 0.0 MAX= 78.0
22/09/82 14.33.00.
Y-PROJ
MIN=-2300.0 MAX= 2100.0
U-PROJ
MIN=-2300.0 MAX= 2100.0
V-PROJ
MIN=-2300.0 MAX= 2100.0
20 22 2 4 6 8 10 12 14 16 18

Fig. 3b

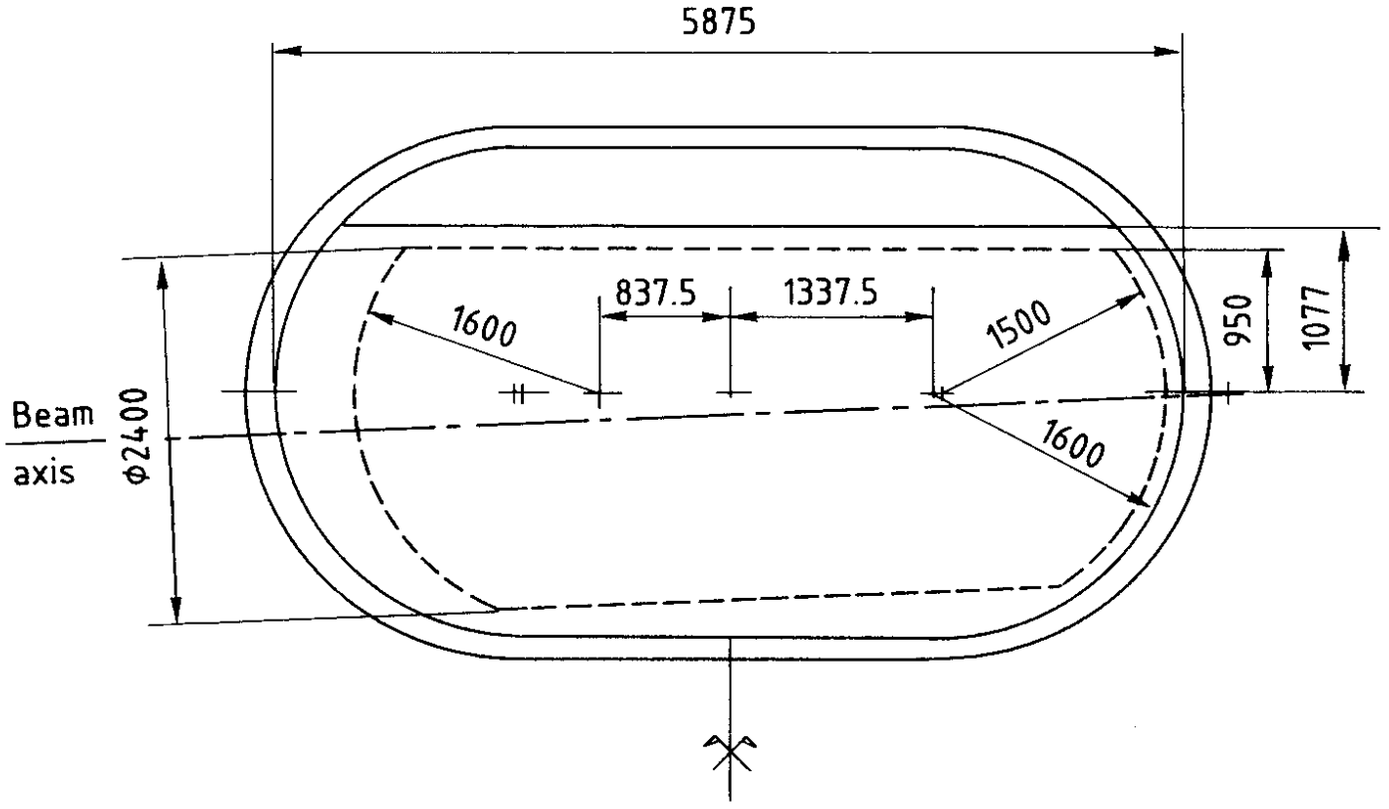

Fig. 4

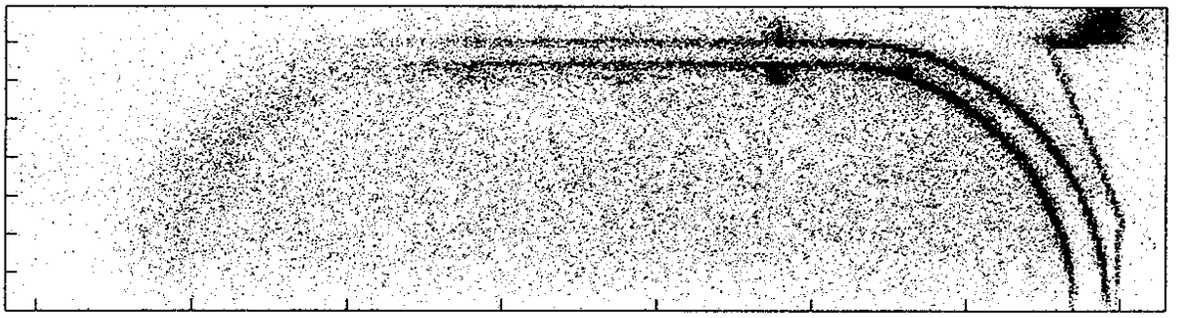

Fig. 5

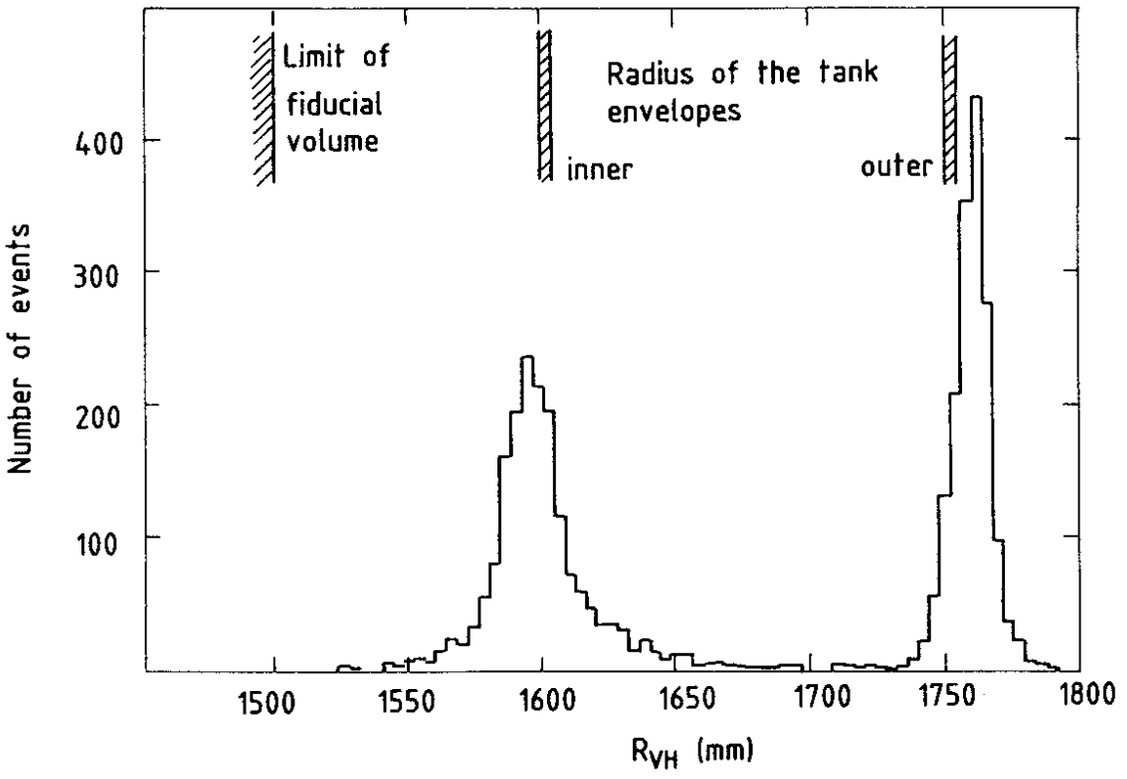
Limit of
fiducial
volume
Radius of the tank
envelopes
inner
outer
Number of events
400
300
200
100
1500
1550
1600
1650
1700
1750
1800
R_{VH} (mm)

Fig. 6

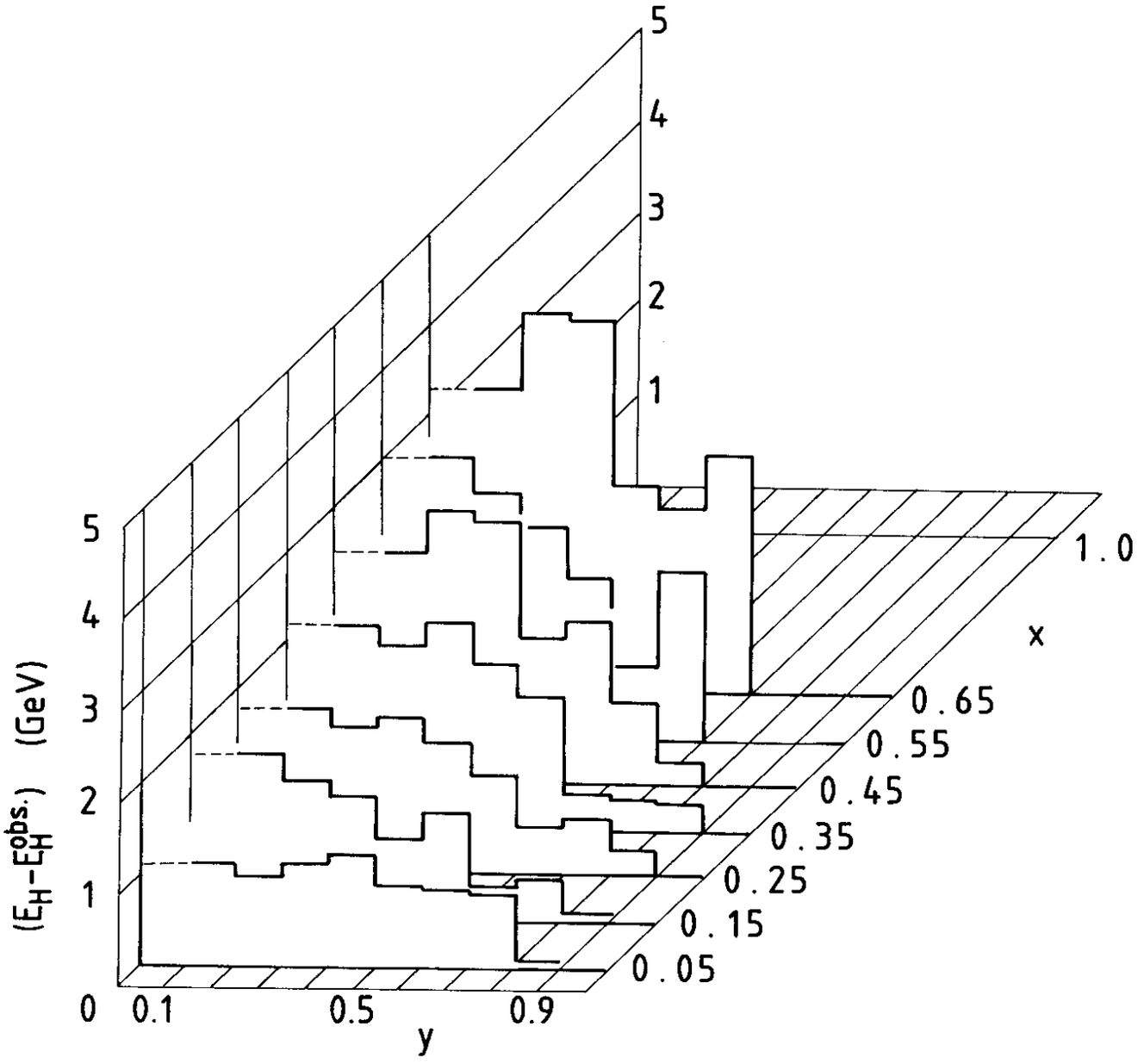

Fig. 7

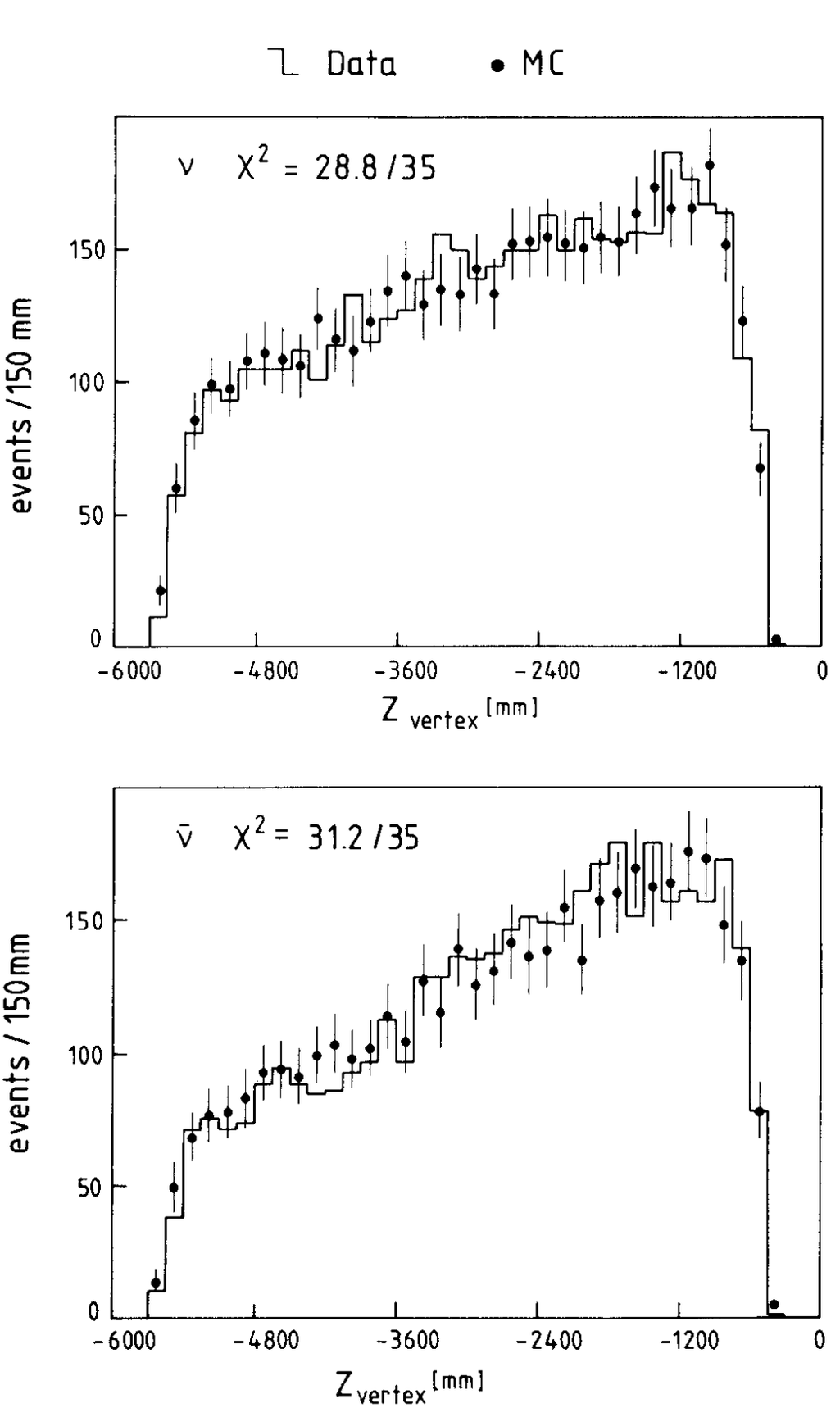
Data
MC
ν
X^2 = 28.8 / 35
events / 150 mm
150
100
50
0
-6000
-4800
-3600
-2400
-1200
0
Z_{vertex} [mm]
$\bar{\nu}$
X^2 = 31.2 / 35
events / 150 mm
150
100
50
0
-6000
-4800
-3600
-2400
-1200
0
Z_{vertex} [mm]

Fig. 8

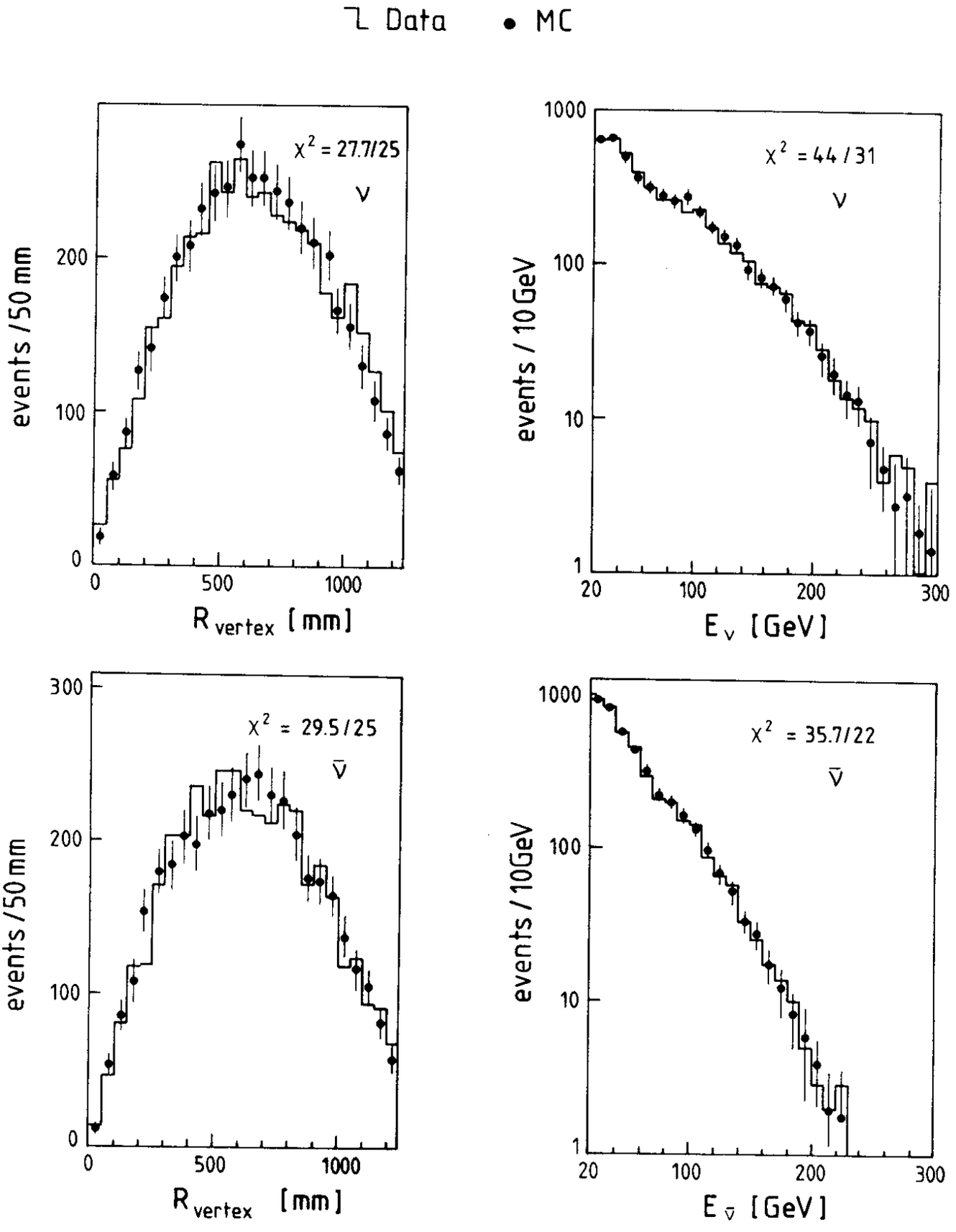
Data
MC
χ^2 = 27.7/25
ν
events /50 mm
R_{vertex} [mm]
χ^2 = 44 / 31
ν
events / 10 GeV
E_ν [GeV]
χ^2 = 29.5/25
$\bar{\nu}$
events /50 mm
R_{vertex} [mm]
χ^2 = 35.7/22
$\bar{\nu}$
events /10GeV
$E_{\bar{\nu}}$ [GeV]

Fig. 9

Fig. 10

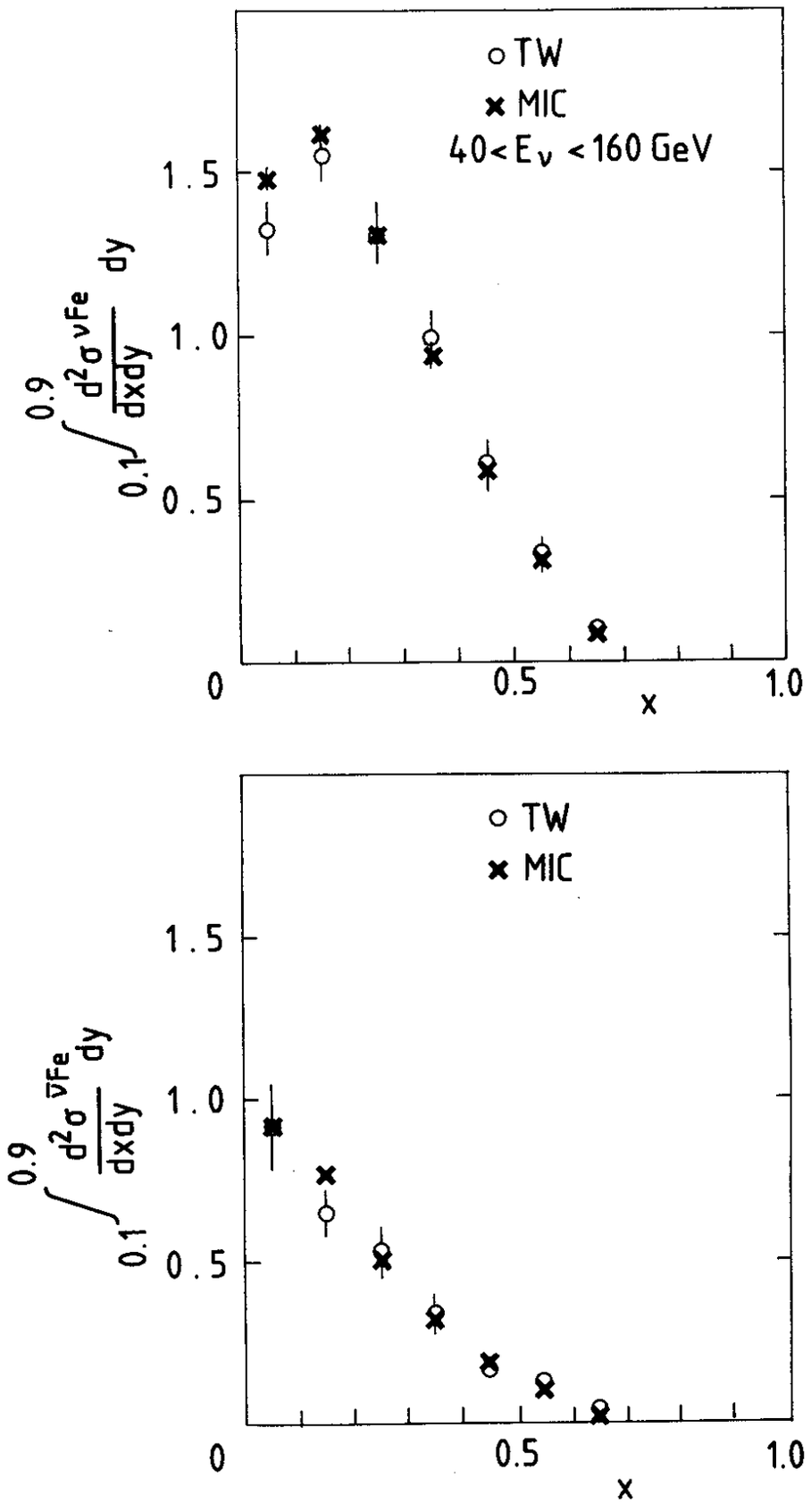
o TW
× MIC
40< Eν <160 GeV
1.5
1.0
0.5
0
0.5
1.0
x
0.9
0.1
d²σ^νFe/dxdy dy
o TW
× MIC
1.5
1.0
0.5
0
0.5
1.0
x
0.9
0.1
d²σ^ν̄Fe/dxdy dy

Fig. 11

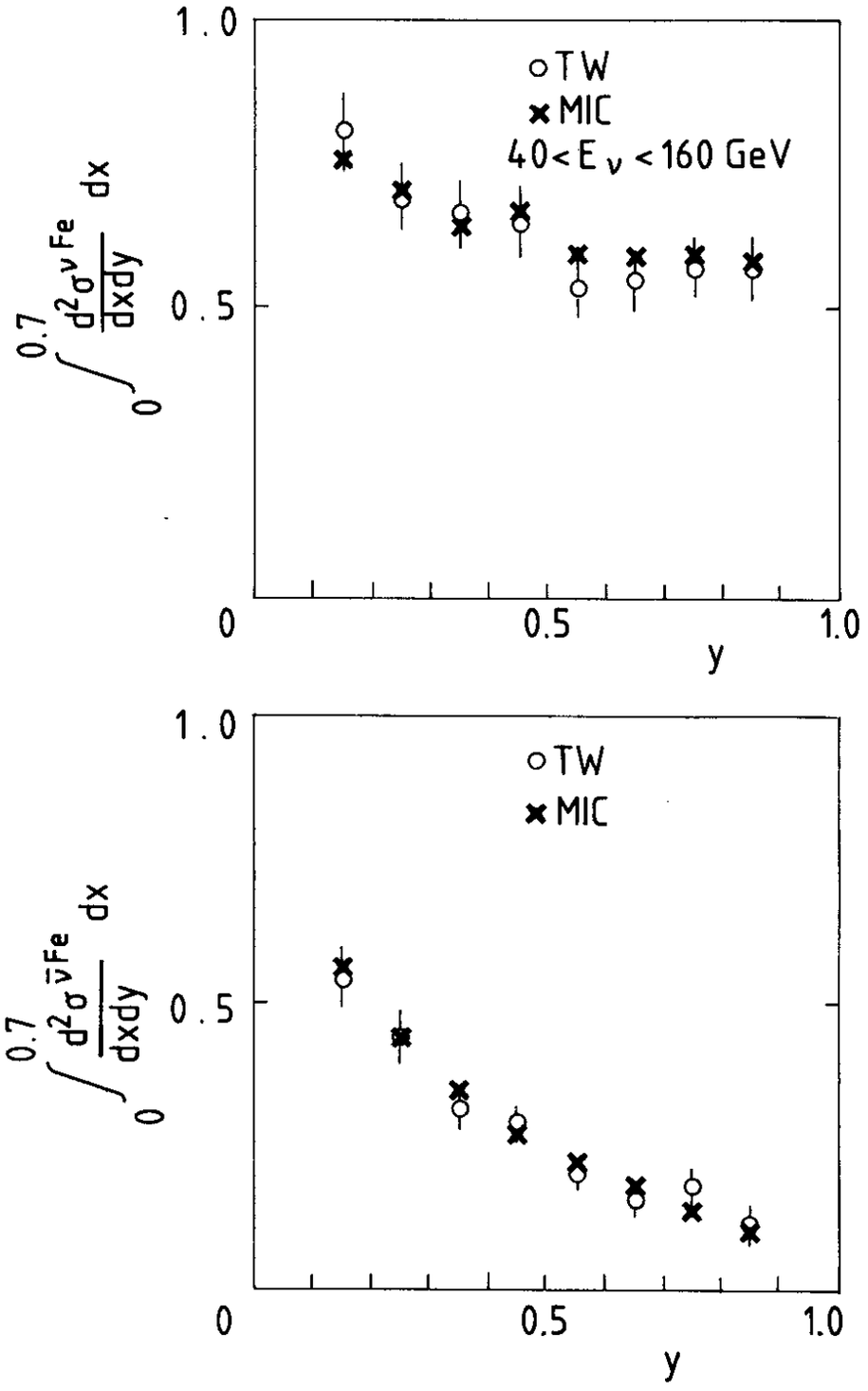
1.0
0.5
0
0.5
1.0
y
TW
MIC
40< E ν < 160 GeV
0.7
∫ d²σ^νFe/dxdy dx
0
1.0
0.5
0
0.5
1.0
y
TW
MIC
0.7
∫ d²σ^ν̄Fe/dxdy dx
0

Fig. 12

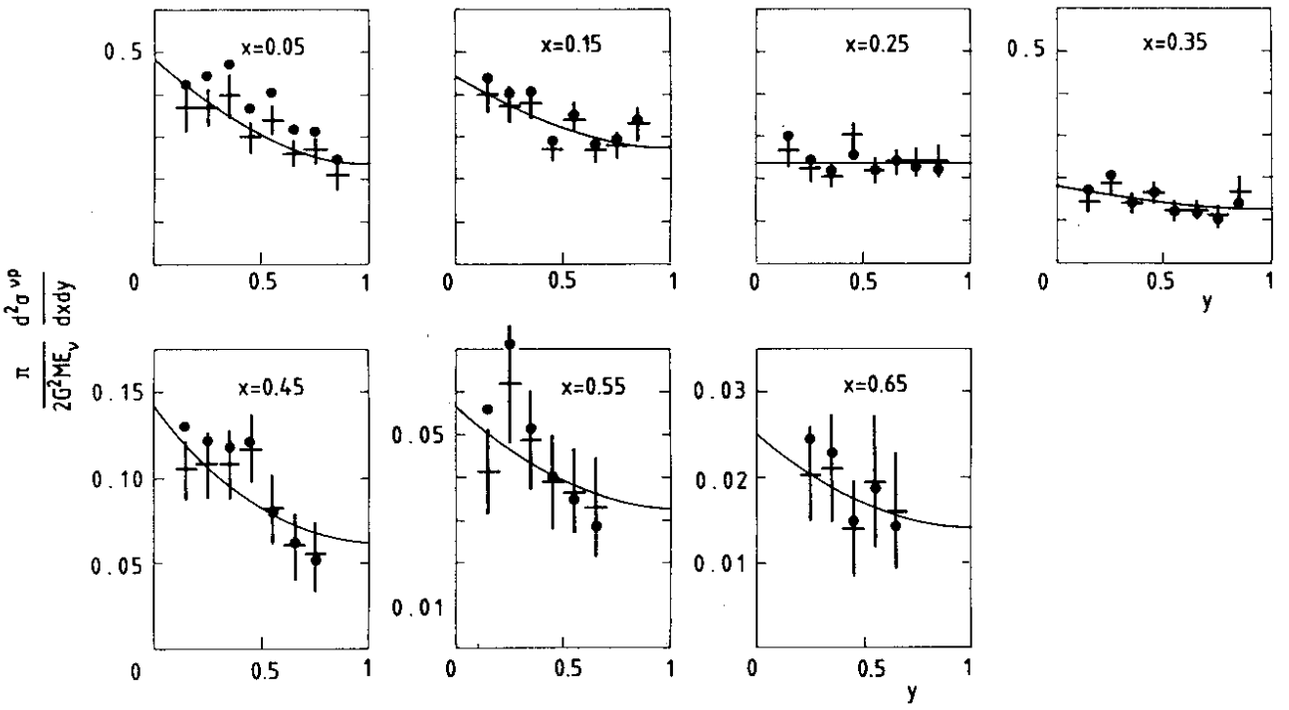
x=0.05
x=0.15
x=0.25
x=0.35
x=0.45
x=0.55
x=0.65
$\frac{\pi}{2G^2ME_\nu}\frac{d^2\sigma^{\nu p}}{dxdy}$
y

a)

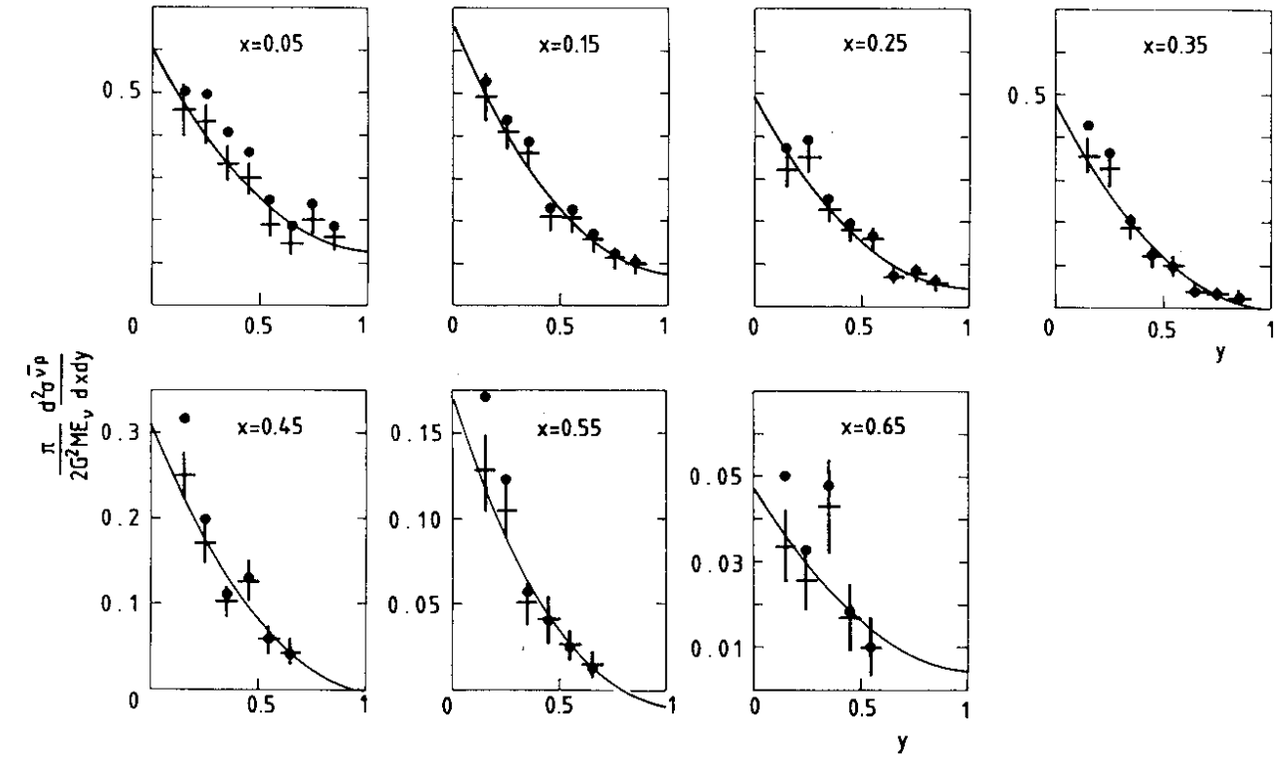
x=0.05
x=0.15
x=0.25
x=0.35
x=0.45
x=0.55
x=0.65
$\frac{\pi}{2G^2ME_\nu}\frac{d^2\sigma^{\bar{\nu}p}}{dxdy}$
y

b)

Fig. 13

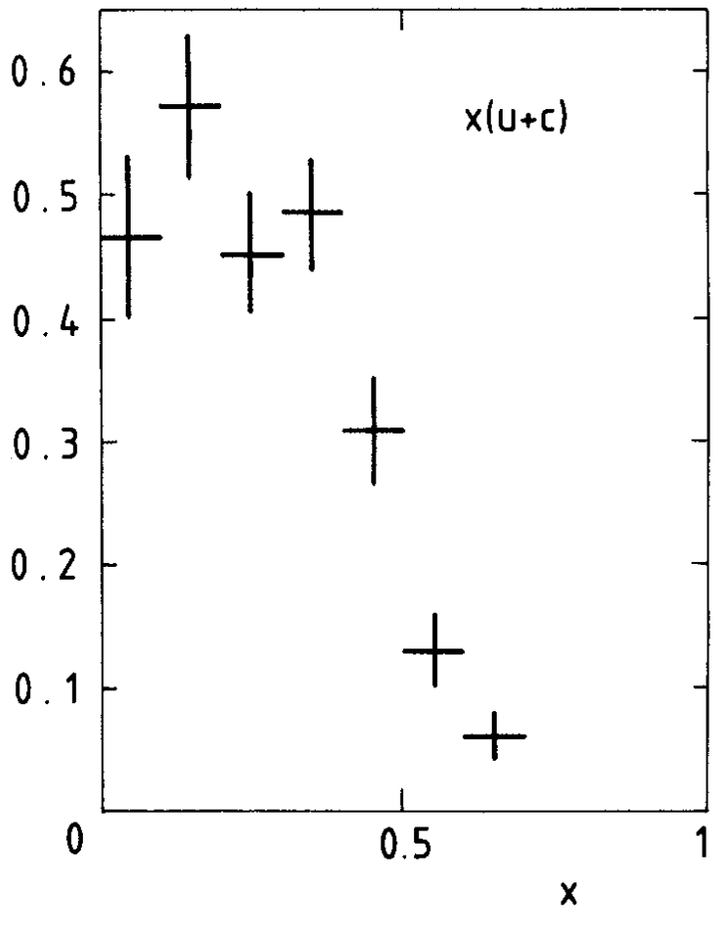

a)

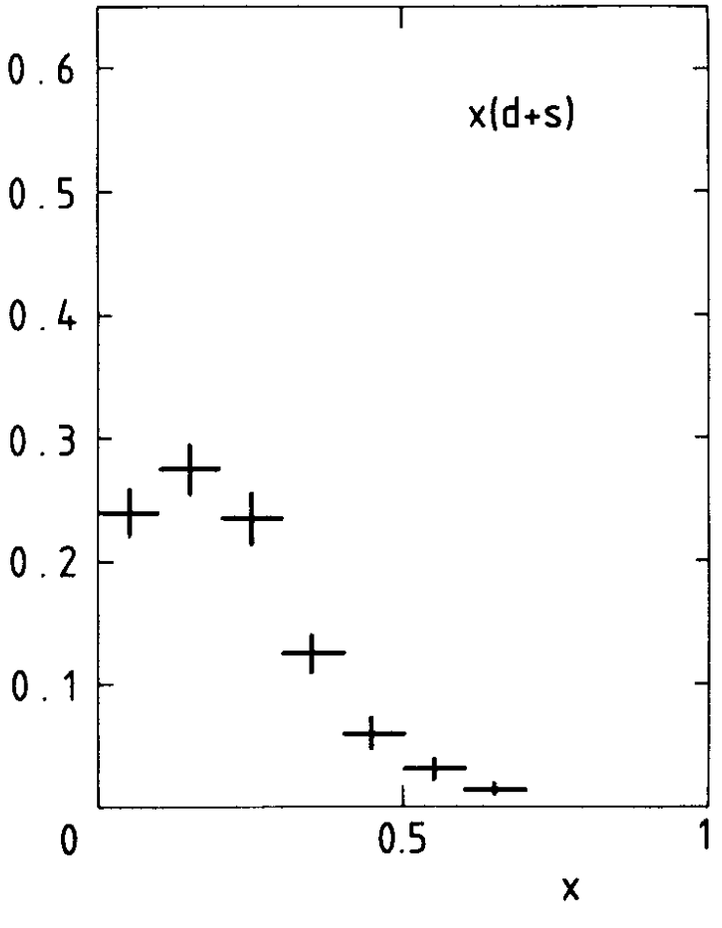

b)

Fig. 14

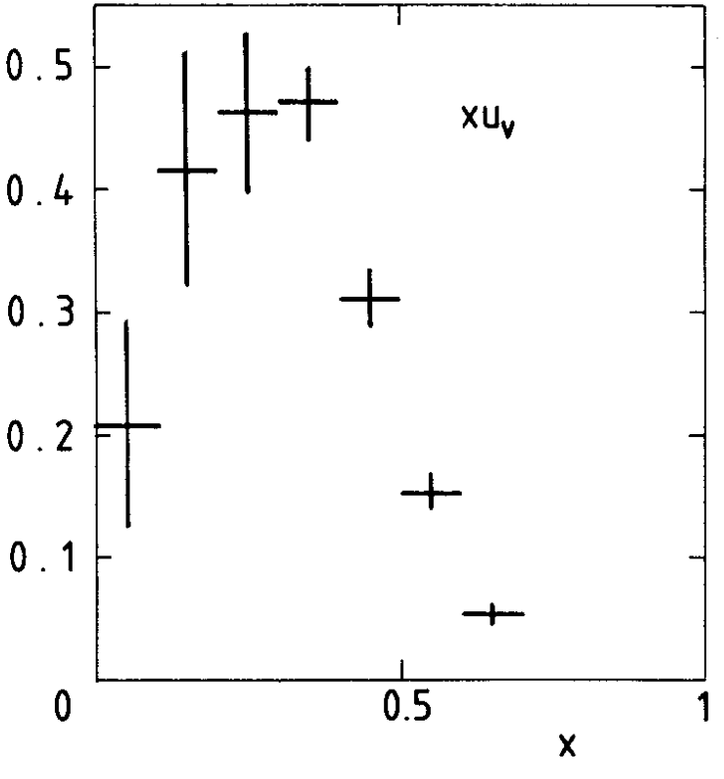

a)

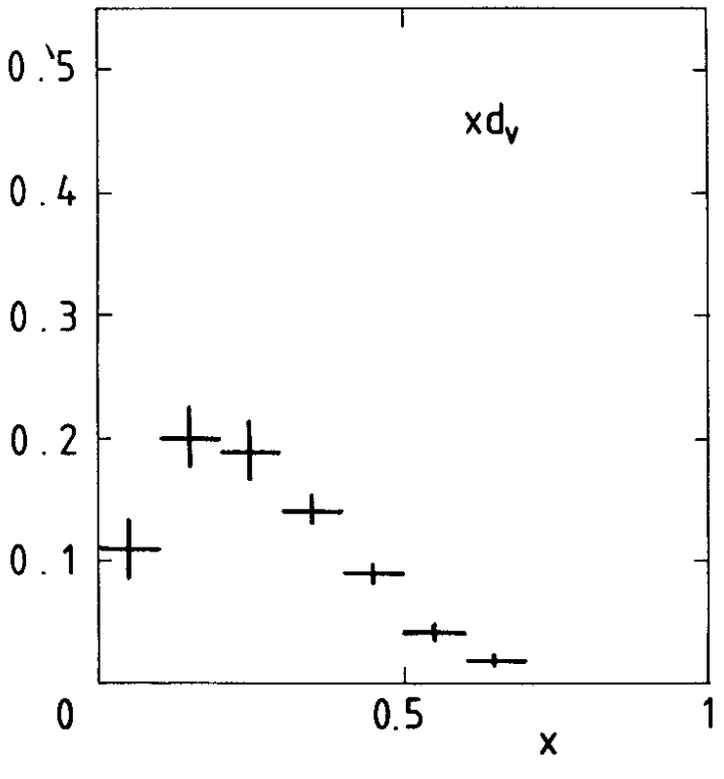

b)

Fig. 15

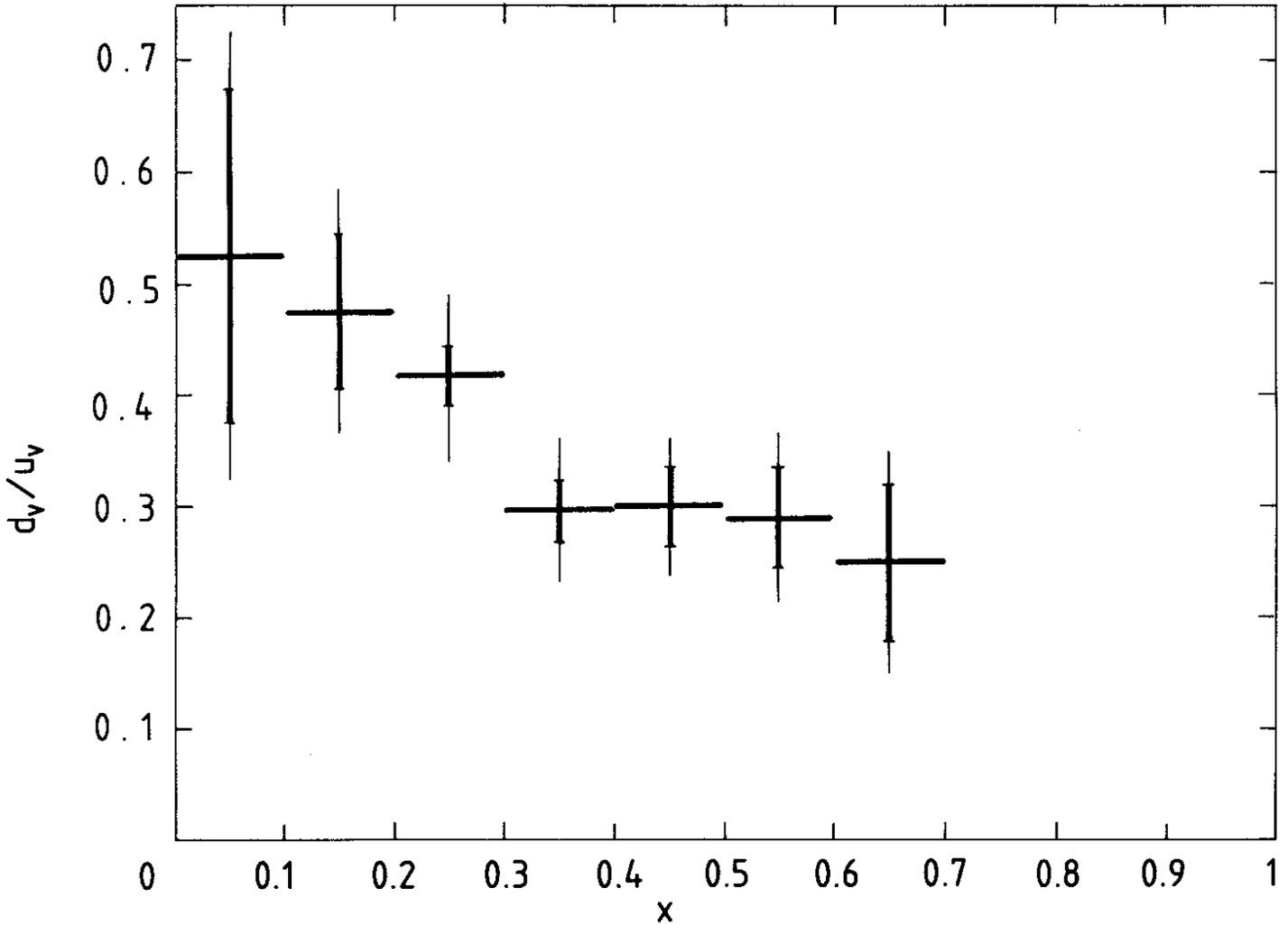

Fig. 16

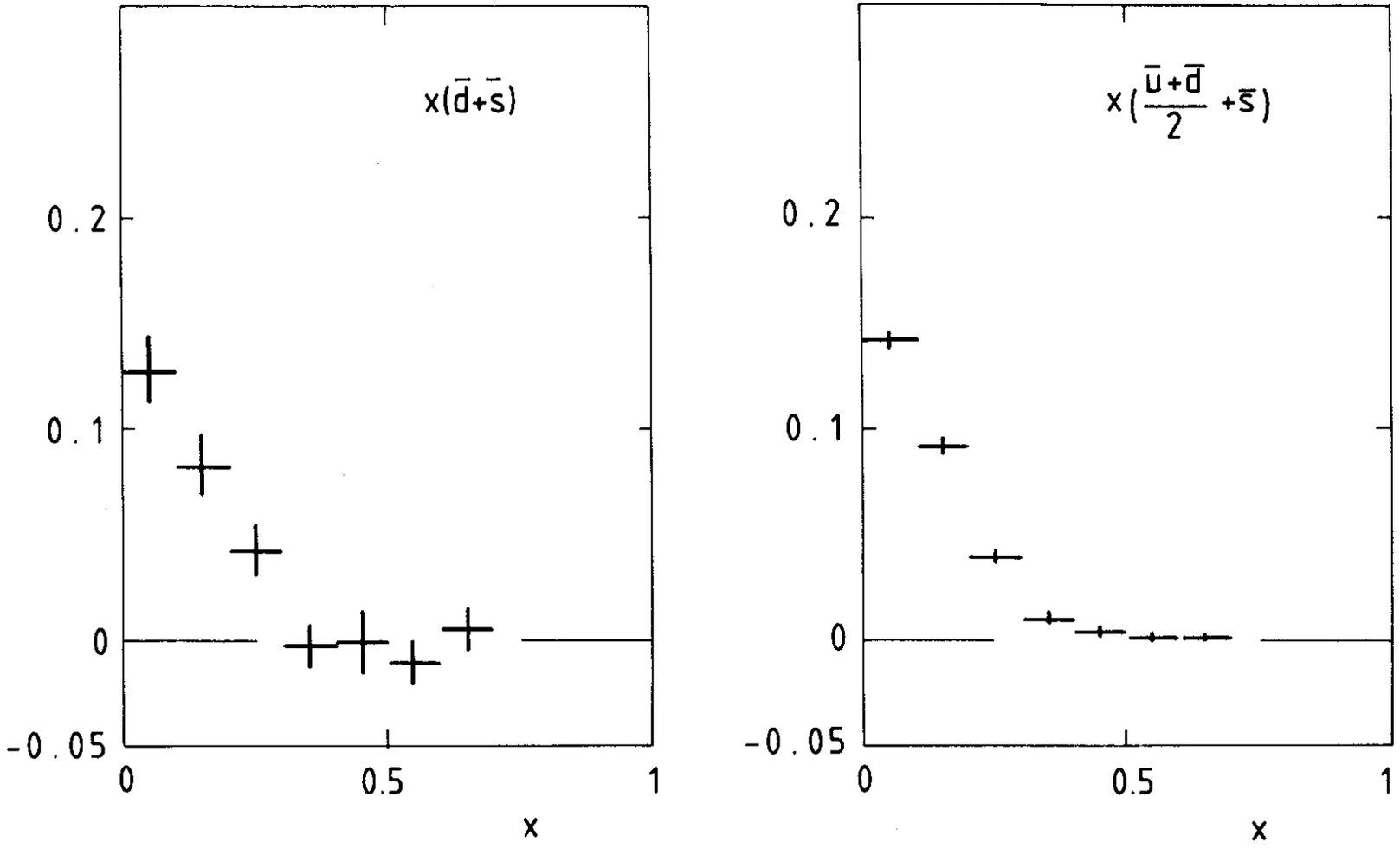

a) b)

Fig. 17

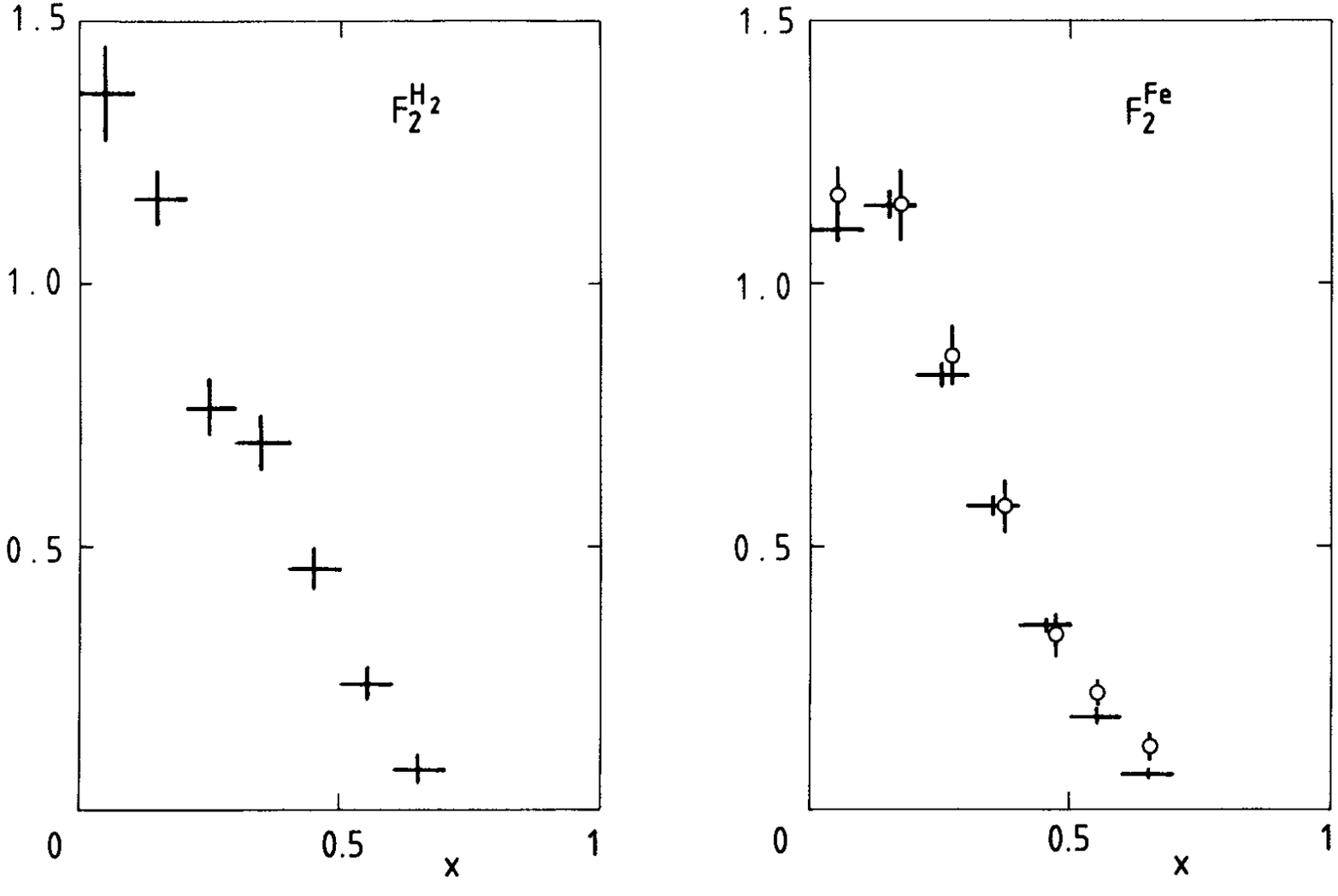

a) b)

Fig. 18

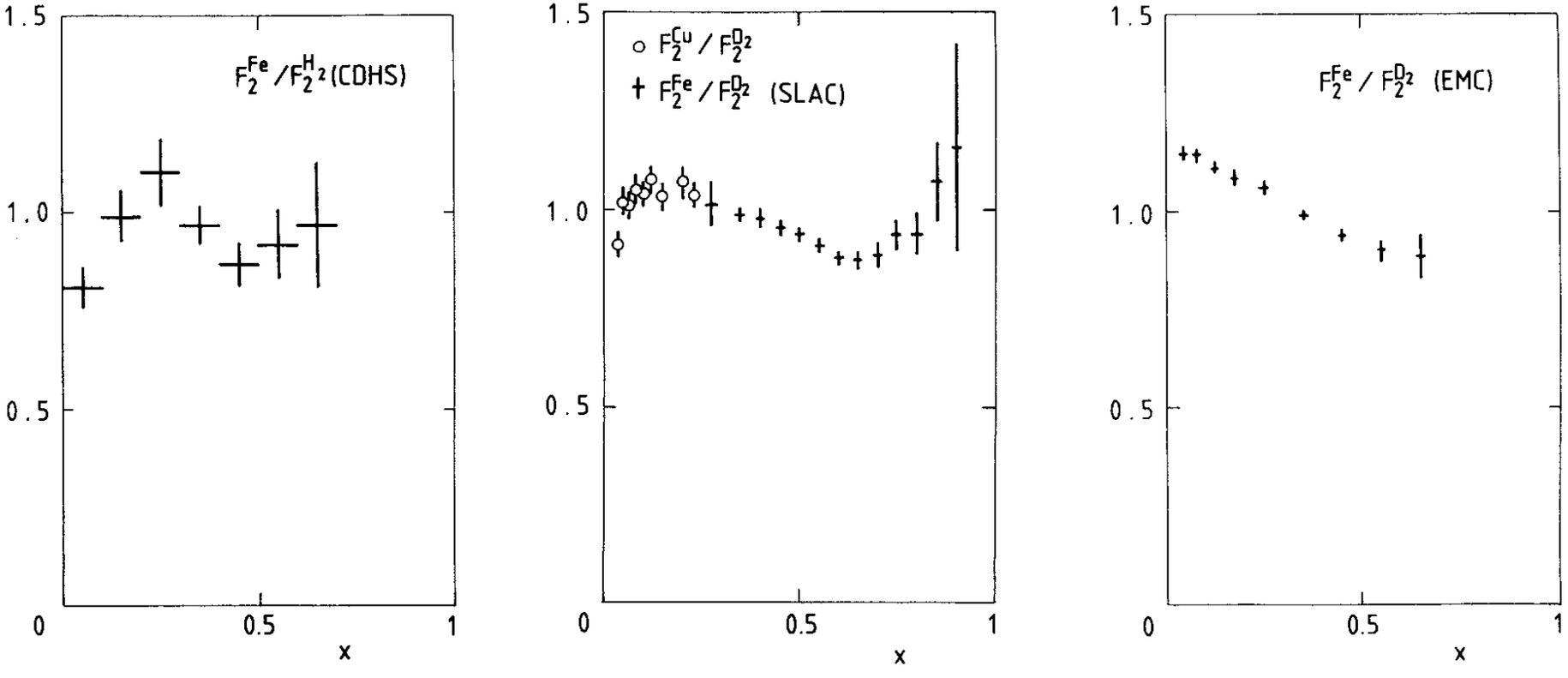
1.5
1.0
0.5
0
0.5
1
x
$F_2^{Fe}/F_2^{H_2}$(CDHS)
$F_2^{Cu}/F_2^{D_2}$
$F_2^{Fe}/F_2^{D_2}$ (SLAC)
$F_2^{Fe}/F_2^{D_2}$ (EMC)

a) b) c)

Fig. 19

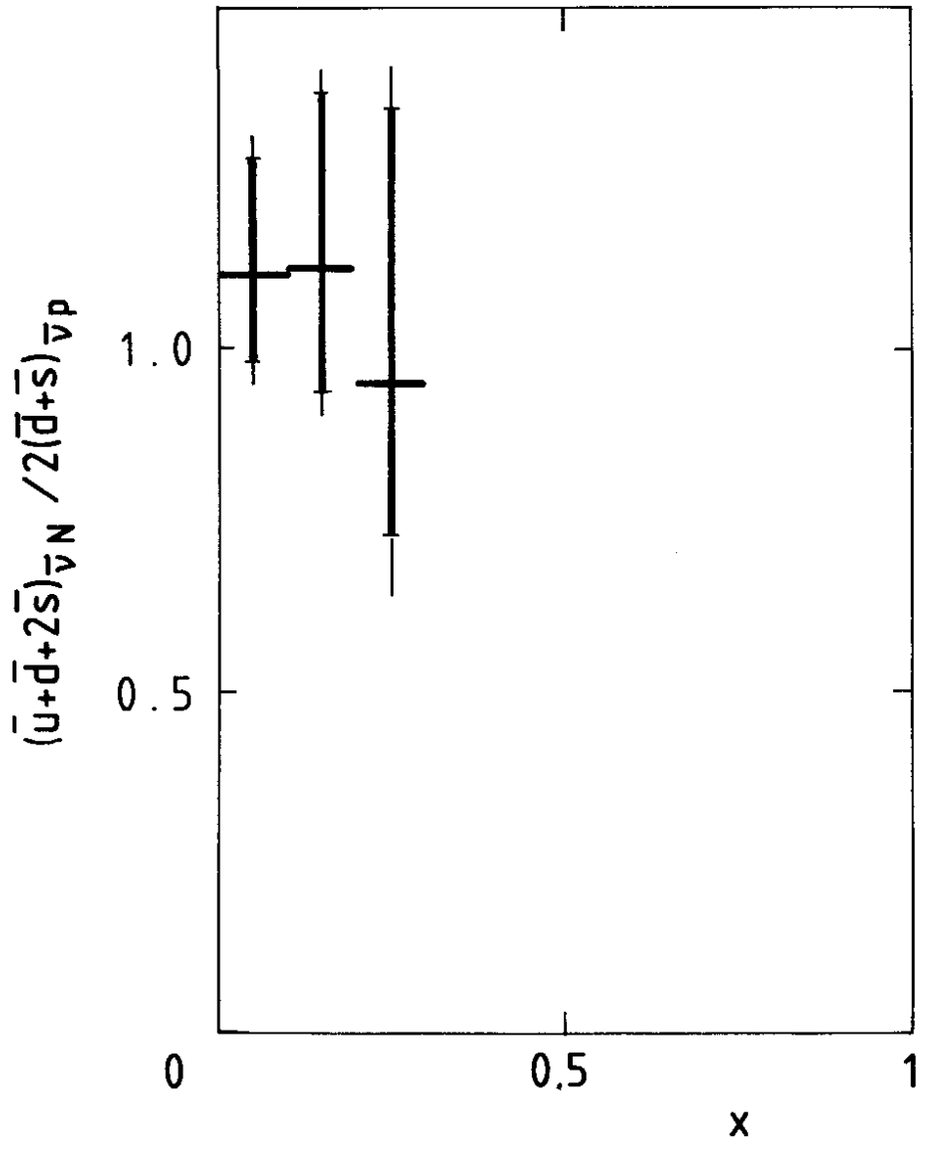

Fig. 20